MODELING STUDY OF PROPOSED FIELD CALIBRATION SOURCE USING

K-40 SOURCE AND HIGH-Z TARGETS FOR SODIUM IODIDE DETECTOR

A Thesis

by

JEREMY LAYNE ROGERS

Submitted to the Office of Graduate Studies of
Texas A&M University
in partial fulfillment of the requirements for the degree of

MASTER OF SCIENCE

Approved by:

Chair of Committee,   Craig M. Marianno
Committee Members,   Stephen B. Guetersloh
                       Sunil P. Khatri
Head of Department,   Yassin A. Hassan

December 2012

Major Subject: Health Physics

ABSTRACT

The Department of Energy (DOE) has ruled that all sealed radioactive sources,

even those considered exempt under Nuclear Regulatory Commission regulations, are

subject to radioactive material controls. However, sources based on the primordial

isotope potassium-40 (^{40}K) are not subject to these restrictions. Potassium-40's beta

spectrum and 1460.8 keV gamma ray can be used to induce K-shell fluorescence x rays

in high-Z metals between 60 and 80 keV. A gamma ray calibration source is thus

proposed that uses potassium chloride salt and a high-Z metal to create a two-point

calibration for a sodium iodide field gamma spectroscopy instrument.

The calibration source was designed in collaboration with Sandia National

Laboratory using the Monte Carlo N-Particle eXtended (MCNPX) transport code. The x

ray production was maximized while attempting to preserve the detector system's

sensitivity to external sources by minimizing the count rate and shielding effect of the

calibration source. Since the source is intended to be semi-permanently fixed to the

detector, the weight of the calibration source was also a design factor.

Two methods of x-ray production were explored. First, a thin high-Z layer (HZL)

was interposed between the detector and the potassium chloride-urethane source matrix.

Second, bismuth metal powder was homogeneously mixed with a urethane binding agent

to form a potassium chloride-bismuth matrix (KBM).

The two methods were directly compared using a series of simulations, including

their x ray peak strengths, pulse-height spectral characteristics, and response to a

simulated background environment. The bismuth-based source was selected as the development model because it is cheap, nontoxic, and outperforms the high-Z layer method in simulation.

The overall performance for the bismuth-based source was significantly improved by splitting the calibration source longitudinally into two halves and placing them on either side of the detector. The performance was improved further by removing the binding agent and simulating a homogeneous mixture of potassium chloride and bismuth powder in a 0.1 cm plastic casing. The split plastic-encased potassium chloride-bismuth matrix would serve as a light, cheap, field calibration source that is not subject to DOE restrictions.

DEDICATION

For my family and dear friends, past, present, and future

ACKNOWLEDGEMENTS

Northwest National Laboratory, for patiently answering my many questions on neutron interactions, coincidence counting, and MCNP modeling.

I want to thank my family for being so unshakably supportive. My life and career paths are completely different than I would have thought six years ago, but you've been there for me through it all.

Finally, I would like to thank my lovely partner and best friend, Kara Polansky. Thank you so much, sweetheart, for your love and patience. You make my life better just by being in it. I hope that we can be in the same city again soon.

NOMENCLATURE

Au	Gold
Bi	Bismuth
BR	Branching Ratio
CAC	Counts Above Continuum
DOE	United States Department of Energy
F1	Surface current tally
F5	Flux at a point or ring tally
F6	Energy deposition tally
F8	Pulse height distribution tally
HZL	High-Z Layer
K	Potassium
KBM	Potassium Chloride/Bismuth Matrix
KBMS	Split Potassium Chloride/Bismuth Matrix source
PKBS	Plastic-encased Split Potassium Chloride/Bismuth source
KCl	Potassium Chloride
MCA	Multi-Channel Analyzer
MCNPX	Monte Carlo N-Particle eXtended
MFP	Mean Free Path
N	Normalization factor for MCNPX tally output
NaI(Tl)	Sodium Iodide (Thallium-doped)

Pb	Lead
PP	Polypropylene
PTFE	Polytetrafluoroethylene (trade name Teflon®)
Ta	Tantalum
T_i	Normalized MCNPX Tally output
USGS	United States Geological Survey
W	Tungsten

TABLE OF CONTENTS

LIST OF FIGURES

LIST OF TABLES

1. INTRODUCTION

1.1.   Background

The U.S. Department of Energy (DOE) has ruled that the exempt sealed radioactive sources, such as those used for energy calibration of gamma ray detection instruments, are still subject to all applicable requirements of 10 CFR 835 (DOE 2007). Therefore, exempt quantities under DOE control are subject to radioactive material controls, transportation and shipping restrictions, and must be disposed as hazardous waste at the end of their lifetime. These restrictions represent substantial additional costs to DOE facilities, especially when transporting calibration sources between buildings or to offsite facilities.

Small calibration sources for gamma spectrometers used in the field are essential for proper radioisotope identification and analysis. These small sources emit gamma rays with known energies and allow users to calibrate the instrument's energy spectrum. When properly calibrated, a gamma detection instrument can be used to find and identify gamma-emitting radioactive materials in the field.

The U.S. Nuclear Regulatory Commission (NRC) permits the possession of "exempt quantities" of certain radioisotopes without requiring a radioactive material possession license (NRC 2008). Calibration sources are virtually always exempt quantities, containing radioactivity levels far below the amount that would lead to adverse health effects. Under NRC regulations, exempt sources do not require training or a possession license, and may be disposed of as regular waste once they have decayed

1

beyond detectability and the radioactive labels have been obliterated (HPS 2010).

However, the DOE has enacted more restrictive policies, requiring special training to

handle exempt sources and to transport radioactive sources offsite.

Furthermore, most exempt quantity calibration sources have an effective life of

only a few years, so they must be disposed of as hazardous materials and replaced

regularly. Those with long effective lives (e.g. ^{137}Cs and ^{60}Co) tend to emit radiation in a

narrow band of energies, making them suitable for calibration only in conjunction with

other sources. See Table 1.1 for a list of common exempt quantity gamma ray sources

and their primary emission energies and intensities.

Table 1.1. Common exempt quantity radioactive sources used for energy calibration and demonstration.

Source Isotope	Half-Life	10 CFR 30.71 Schedule B Exempt Quantities (µCi)	Gamma Energies (keV)	Gamma Yield (%)
^{133}Ba	10.7 a	10	81.0	32.8
			276.3	7.3
			302.7	18.6
			355.9	62.3
			383.7	8.8
^{109}Cd	453.4 d	10	88.0	3.8
^{137}Cs	30.1 a	10	32.2	3.7
			661.6	84.6
^{57}Co	270 d	100	14.4	9.5
			122.1	85.6
			136.4	10.6
^{60}Co	5.3 y	1	1173.2	99.9
			1332.5	99.9
^{54}Mn	312.2 d	10	834.8	99.9
^{22}Na	2.60 y	10	511.0	179.8
			1274.5	99.9

Calibration sources may also be made from naturally occurring radioactive material (NORM). NORM sources, which include unprocessed uranium and thorium ores and ^{40}K, are not subject to DOE restrictions, though there are several NRC restrictions on ores. Uranium and thorium ores produce gamma ray emissions of various energies, mostly through the decay of their daughter products.

However, unprocessed uranium and thorium ores would be difficult to implement as calibration sources. Depending on whether the source has been chemically separated, the daughter products may or may not be decaying in equilibrium with the parents, leading to fewer gamma ray emissions and difficulties in characterizing the source. Both uranium and thorium ores include isotopes of radon as part of their respective decay chains, and are thus potentially hazardous if kept in an enclosed and poorly-ventilated storage location. Another problem with using these ores as calibration sources is quality control: variances in elemental and isotopic composition between individual sources would make characterizing each unique source a necessity. Finally, these sources would be relatively large. Attempting to reduce their physical size through chemical concentrations would result in their being classified as Technologically Enhanced Naturally Occurring Radioactive Materials (TENORM), which could make them subject to radioactive material restrictions.

NORM sources made from the primordial isotope ^{40}K do not share the same difficulties in characterization. ^{40}K makes up a constant 0.0117% of natural potassium, an abundance that appears to be constant to within 1-1.5% throughout North America (Burnett et al. 1966, Begemann et al. 2001). The use of ^{40}K is not currently regulated by

the DOE, meaning its use in calibration sources could potentially save money on training and transportation costs.

^{40}K has a half-life of 1.248×10^9 years and decays by two modes. 89.28% of the time, it decays through the emission of a beta particle to stable ^{40}Ca. This beta particle has a maximum energy of 1311.07 keV and an average energy of 560.18 keV. In the remainder of its decay events, ^{40}K decays through electron capture to stable ^{40}Ar. The vast majority of the time (99.44%), ^{40}Ar is created in an excited state and emits a 1460.822 keV gamma ray to reach the ground state (NNDC 2004). Since ^{40}K is ubiquitous in terrestrial soil, this gamma ray appears as a small peak in virtually any spectral measurement. See Fig. 1.1 for the ^{40}K decay scheme.
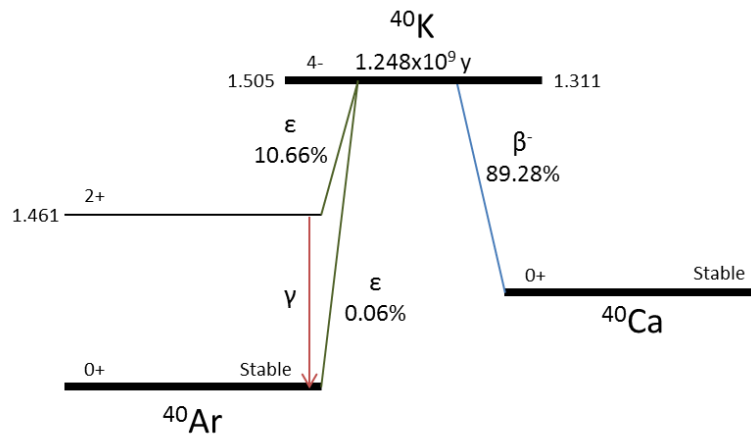
Fig. 1.1. The ^{40}K decay scheme (NNDC 2004).

Using ^{40}K as a gamma ray calibration source has two potential disadvantages.

First, because of ^{40}K's long half-life and low natural abundance, a relatively large

amount of natural potassium is needed to produce a measureable gamma ray signal in

the detector. Calibration sources containing potassium will thus be physically larger than

standard exempt sources, which are generally assumed to be point sources with minimal

self-attenuation. These assumptions would not hold for a potassium-based source.

Second, field gamma spectrometers require at least two photon signals widely spaced in

energy for proper calibration, to account for NaI's nonlinear energy response. Placing a

material with high atomic number (above 70) in contact with the potassium source may

solve this issue. Electron interactions in high-Z materials result in the emission of

characteristic K-shell x rays between 59 keV and 75 keV, depending on the target

material (see Section 2). These x rays can be used to provide a low-energy x ray peak to

provide a rapid two-point field calibration.

1.2.   Research and Development

This work, in collaboration with Sandia National Laboratory, seeks to design and

optimize a calibration source that uses NORM not subject to current DOE restrictions.

The use of potassium chloride (KCl) salt, which is weakly radioactive due to the

presence of primordial ^{40}K, is not restricted.

The calibration source design will optimize the production of the low-energy x

ray peak while avoiding the use of DOE-restricted radioactive and hazardous materials.

The design also seeks to minimize the materials and productions costs, and the physical

size of the source. Since the calibration source is meant for use as a permanent or semi-permanent fixture on the spectrometer, the source design will seek to maximize the detector sensitivity by reducing the calibration source's contribution to the total count rate and shielding effect on external photons.

This source will be used as a semi-permanent or removable, two-point energy calibration source, and if possible, as a permanently-fixed gain stabilization source. Efficiency calibrations with this source would be difficult, though not impossible.

This calibration source will be able to operate without transportation and handling restrictions, and will not require disposal because of ^{40}K's long radioactive half-life. The lifetime of a ^{40}K-based calibration source for a gamma spectrometer will be limited only by the aging of the NORM-containing matrix.

1.3. Objectives

This thesis details the development of a calibration source in conjunction with Sandia National Laboratory that uses unrestricted use NORM to provide multiple calibration points for field energy calibration. The NORM source will be made from commercially available potassium chloride salt bound up in a urethane matrix. The source will also include a high-Z material, where x rays will be produced through interactions with ^{40}K's beta and gamma radiation. The primary objectives of this work are to use the MCNPX radiation transport code to simulate and optimize the production of K-shell x rays in high-Z materials recorded by a NaI(Tl) detector.

Two methods of producing x rays will be explored in this work. The first uses KCl salt in a urethane binding matrix to induce x rays in a thin (order of μm) high-Z metal layer electroplated onto the surface of the detector casing. This is referred to as the High-Z Layer (HZL) method. The second uses a homogeneous mixture of KCl salt and bismuth metal powder in a urethane binding matrix. This method is referred to as the KCl-bismuth matrix (KBM). The characteristics of the simulated pulse-height spectra from each method will be compared, and the most favorable calibration source will be selected based on the parameter space explored.

2.   INTERACTIONS AND APPLICATIONS

2.1.   Electron Interactions in Matter

Electrons are subatomic, negatively-charged particles. Free electrons, like the

beta particles emitted by ^{40}K, slow down and lose their kinetic energy through complex,

Coulomb-force interactions with other atoms. The nature of the interactions is based on

the relationship between the impact parameter b, and the classical atomic radius a (Attix

2004). The two parameters are illustrated in Fig. 2.1.
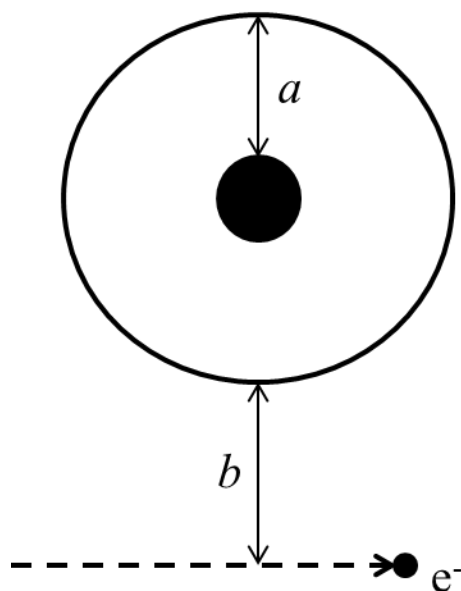
Fig. 2.1. The impact parameter b is the measure of how closely a free electron passes by
an atom with classical atomic radius a.

In "soft" collisions, the electron passes by the atom at a relatively large distance

($b \gg a$). The free electron's Coulomb field slightly distorts the atomic electrons and

excites them to a higher energy level. Rarely, soft collisions lead to atomic ionizations

8

by ejecting a valence-shell electron. The net effect is a small transfer of energy from the electron to the atom. Soft collisions are the most probable type of interaction and account for roughly half of the energy transfer to the surrounding matter (Attix 2004).

In "hard" or "knock-on" collisions, the free electron's path takes it near the dimensions of the atomic radius ($b \sim a$). In this case, the free electron is much more likely to interact directly with one atomic electron, ejecting it from its shell and transferring some amount of kinetic energy. The ejected electron is called a δ ray, which must dissipate its own kinetic energy through charged-particle interactions. It is impossible to discriminate between the incident electron and the δ ray after interaction; by convention, the δ ray is defined as the electron with less kinetic energy after the reaction (Attix 2004). This can lead to the emission of a fluorescence x ray or an Auger electron cascade.

When the electron passes well inside of the atomic electrons ($b \ll a$), it interacts directly with the nuclear Coulomb field. Nuclear Coulomb-force interactions are much more probable in high-Z materials, as the cross-section increases with Z^2. In the vast majority of these interactions (97-98%), the electron undergoes elastic scattering and loses a tiny fraction of its kinetic energy. In the remainder of the nuclear interactions, the electron loses a significant portion of its kinetic energy as it changes direction, and must emit a photon (known as bremsstrahlung) to fulfill the conservation of energy. The electron may lose up to all of its energy to the bremsstrahlung photon, though this is rare (Attix 2004).

Electrons thus may lose their kinetic energy by either collisional or radiative (bremsstrahlung) means. The total mass stopping power of an electron in matter is given by

$$\frac{dT}{\rho dx} = (\frac{dT}{\rho dx})_c + (\frac{dT}{\rho dx})_r \qquad (2.1)$$

where $dt \, \rho^{-1} \, dx^{-1}$ is the mass stopping power, and the subscripts c and r represent the collisional and radiative terms, respectively. The ratio of radiative to collisional stopping power is given by

$$\frac{(dT/\rho dx)_r}{(dT/\rho dx)_c} \cong \frac{TZ}{n} \qquad (2.2)$$

where T is the electron kinetic energy, Z is the atomic number of the target medium, and n is a constant. The relative importance of radiative stopping power therefore increases with more energetic electrons and higher-Z materials (Attix 2004). This relation is the main reason for the selection of high-Z materials to function as the x ray production materials.

Defining the range of most heavy charged particles is fairly straightforward, as they tend to move in a straight line for most of their particle track. Defining electron range is not so simple because electrons often follow tortuous tracks. Range calculations for electrons often use the assumption of straight-ahead travel for conservatism, which overestimates the electron penetration for the vast majority of incident electrons. The collisional stopping power for electrons is reduced in high-Z media, but this difference is more than compensated for by the radiative stopping power, resulting in shorter electron ranges in materials with higher Z (Turner 2007).

2.2. Photon Interactions

Photons impart energy through three primary mechanisms: the photoelectric effect, the Compton effect, and pair production (Evans 1955). All three mechanisms create free electrons, which may have enough energy to create their own bremsstrahlung and fluorescence x rays. Thus, photons can indirectly create x rays as they interact with matter.

The photoelectric effect describes the interaction between a photon and a bound electron, where the photon deposits its entire energy into the ionization of the electron. The electron is given a kinetic energy T given by

$$T = h\upsilon - E_b \tag{2.3}$$

where $h\upsilon$ is the incident photon energy, and E_b is the potential energy of the bound electron. Since the photon energy is completely absorbed, the electron's kinetic energy is independent of its scattering angle. The photoelectric effect dominates at low photon energies, especially in high-Z materials, whose electrons are less tightly bound (Attix 2004). The photoelectric effect is the most common interaction in photon spectrometers because virtually the entire photon energy is deposited in the medium.

The Compton effect describes the interaction where a photon imparts only a part of its energy to an electron, which is assumed to be unbound and stationary. Since both the photon and the electron are scattered by this process, the kinetic energy of each are described by a distribution of energies dependent on the scattering angle. The kinematics of the Compton scattering interaction can be described in three basic equations:

$$E' = \frac{E}{1+(\frac{E}{m_0 c^2})(1-cos\,\varphi)} \tag{2.4}$$

$$T = E - E' \tag{2.5}$$

$$cot\,\theta = (1 + \frac{E}{m_0 c^2})(tan\frac{\varphi}{2}) \tag{2.6}$$

where E is the initial photon energy, E' is the scattered photon energy, $m_0 c^2$ is the rest electron mass (511 keV), T is the recoil electron energy, ϕ is the scattered photon angle, and θ is the recoil electron angle (Attix 2004).

These formulas indicate two extreme events in Compton scattering. In the first, the electron gains a negligible amount of energy from the photon, which continues with virtually no change in energy or direction. The second involves the photon imparting the maximum amount of energy to the electron, which recoils in the forward direction, while the photon scatters at an angle of 180° to its incident path (Attix 2004). This "backscattered" photon does not impart its full energy to the electron.

A third type of photon interaction, pair production, occurs at energies well above 1.022 MeV. Pair production involves the creation of an electron-positron pair in a nuclear Coulomb field. When the pair loses their kinetic energy, they annihilate and emit two 511 keV photons in opposite directions. Pair production requires a threshold energy of 1.022 MeV, but it does not become a significant interaction until the photon energy reaches ~4 MeV (Evans 1955). The occurrence of pair production with 1460.8 keV gamma rays is so low as to be negligible, so it is not considered throughout the remainder of this work.

All of these interactions impart energy to δ-ray electrons, which may undergo soft and hard collisions, and emit bremsstrahlung and fluorescence x rays as they lose their kinetic energy. Gamma rays thus indirectly produce x rays through the intermediate step of imparting energy to electrons. X ray production from gamma rays is an important component due to their penetrating power, but it is not as efficient as x ray production from direct electron interactions.

The mean free path is used as the unit of thickness for the KBM matrix and the high-Z metal layer. The mean free path is defined as the average distance a single uncharged particle of given energy will travel through a given attenuating medium before interacting with another particle (Attix 2004).

$$mean\ free\ path\ (mfp) = \frac{1}{\mu} \tag{2.7}$$

where μ is the linear attenuation coefficient, which usually has units of cm^{-1}. Dividing by the density of the medium gives μ/ρ, the mass attenuation coefficient. The mean free path thus provides a method for direct comparison of different materials.

2.3. X Ray Production

In hard collisions and photoelectric interactions, the emission of a δ ray from a non-valence atomic electron shell leaves a void that is quickly filled by a higher-shell electron, reducing the potential energy in the atom. The excess energy is removed through x ray fluorescence or an Auger electron cascade. Only a tiny fraction (≤1%) of the electron energy transferred through hard collisions goes into fluorescence x ray production; the rest goes into heating of the electron shell (Attix 2004).

13

The K-shell binding energy, $(E_b)_K$, is the minimum energy that can be applied to remove a K-shell electron. This energy can be supplied through hard electron collisions, the photoelectric effect, or Compton interactions. After the emission of the δ ray and the creation of the K-shell vacancy, the higher-shell electron that fills the shell emits an x ray with quantum energy equal to the difference between the two energy levels involved. The most likely transitions by quantum mechanical selection rules are $L_{III} \rightarrow K$ and $L_{II} \rightarrow K$. These two transitions are named $K_{\alpha 1}$ and $K_{\alpha 2}$, respectively. Since the two are often separated by only a few keV, NaI(Tl) detectors cannot resolve these two x ray peaks, and they will be referred to collectively as the $K_{\alpha 1}$ x ray throughout the remainder of this work. The energies of these transitions for the high-Z metals under consideration, along with their relative yields, are listed in Table 2.1.

Table 2.1. X ray transitions and yields for $Z = 73$, 74, 79, 82, and 83 (Firestone 2004).

Material	Z	Transition	Energy (keV)	X Ray Yield per 100 K-Shell Vacancies
Ta	73	$L_{III} \rightarrow K$ ($K_{\alpha 1}$)	57.535	47.7
		$L_{II} \rightarrow K$ ($K_{\alpha 2}$)	56.280	27.4
W	74	$L_{III} \rightarrow K$ ($K_{\alpha 1}$)	59.318	47.6
		$L_{II} \rightarrow K$ ($K_{\alpha 2}$)	57.981	27.4
Au	79	$L_{III} \rightarrow K$ ($K_{\alpha 1}$)	68.806	47.0
		$L_{II} \rightarrow K$ ($K_{\alpha 2}$)	66.991	27.6
Pb	82	$L_{III} \rightarrow K$ ($K_{\alpha 1}$)	74.969	46.8
		$L_{II} \rightarrow K$ ($K_{\alpha 2}$)	72.805	27.8
Bi	83	$L_{III} \rightarrow K$ ($K_{\alpha 1}$)	77.107	46.8
		$L_{II} \rightarrow K$ ($K_{\alpha 2}$)	74.815	27.8

The fluorescence and bremsstrahlung production processes differ in their directional distributions. Since fluorescence is a secondary process that follows a primary ionization event, fluorescence x rays are emitted isotropically from their source atoms. Bremsstrahlung x rays, however, are emitted to conserve the momentum of a charged particle as it slows and changes direction. They are thus emitted anisotropically, with the photons being emitted primarily in the initial electron direction (Attix 2004).

In thick targets, x rays are filtered by their production medium. Low-energy x rays do not penetrate as well as higher-energy x rays, so they are preferentially attenuated and absorbed before reaching the detector crystal. For this reason, bremsstrahlung often appears as a high-energy tail in gamma spectrometers (Attix 2004). The fluorescence x ray peak and bremsstrahlung tail are visible in Fig. 2.2, which was simulated in MCNPX by a ^{40}K beta spectrum incident on a 0.015 cm gold layer and recorded in a NaI(Tl) crystal. In addition to the attenuation provided by the calibration source material itself, the x rays are also filtered through 1.0 cm of polytetrafluoroethylene (PTFE) and 0.1 cm of stainless steel before reaching the NaI(Tl) crystal where the signal can be recorded.
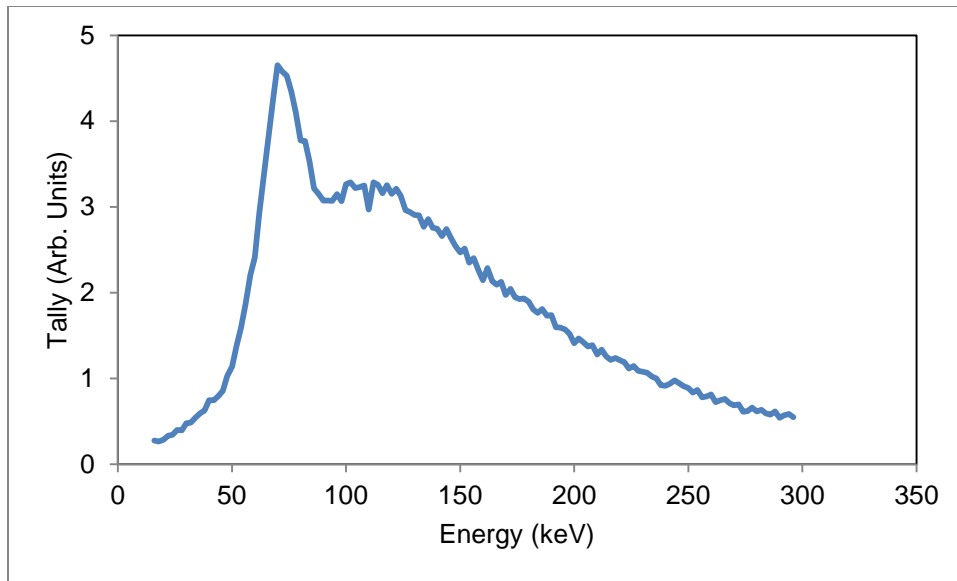
Fig. 2.2. MCNPX output x ray spectrum of ^{40}K beta spectrum incident on 0.015 cm of gold.

A series of filters are often used to remove the bremsstrahlung spectrum and leave only a narrow range of x ray energies around the fluorescence peak. These filtered x ray spectra are useful for characterizing medical x ray beam exposure. However, heavy filtration of the x ray spectrum also greatly reduces the amplitude of the fluorescence peak, necessitating the need for more x ray production in order to achieve the same flux. This would require much more potassium than is practical for a field calibration source, which is already limited by self-shielding. Heavy x ray filtration is thus not practical for this calibration source, but the filtration phenomenon still affects the output.

16

2.4.   Fundamentals of Gamma Scintillation Spectroscopy

Since gamma rays are uncharged, penetrating particles, they are not detected directly. Rather, gamma detectors rely on photon interactions in the detection material that ionize electrons, which impart their energy through excitation and ionization in the detection material, which creates a signal. One class of gamma detectors relies on the scintillation of its detection material to create signal. Of these scintillators, sodium iodide crystals activated by thallium [NaI(Tl)] have been the most successful (Knoll 2000).

Sodium iodide detectors consist of a scintillating NaI(Tl) crystal attached to a photocathode, which converts the UV scintillation light to photoelectrons. The photoelectron signal is amplified in a photomultiplier tube (PMT), which contains a cascade of dynodes that multiply and accelerate the photoelectrons through an applied electric field. These amplified electrons provide the measured signal in the detector (Knoll 2000). The amplitude of the signal is directly proportional to the number of photoelectrons produced, which is directly proportional to the amount of UV scintillation light, which is directly proportional to the energy of the incident photon. This proportionality of response makes spectroscopy possible. Using a multi-channel analyzer (MCA) to sort the signals into bins based on signal strength results in a pulse-height spectrum like that in Fig. 2.3.

Ideally, the peaks in the Fig. 2.3 spectrum would appear as Dirac delta functions. However, the peaks all have a finite width that tends to grow broader with increasing energy. The width is defined as the energy resolution R by

$$R = \frac{FWHM}{H_0} \tag{2.8}$$

where *FWHM* is the full width at half maximum of the full-energy peak, and H_0 is the

mean pulse height corresponding to the same peak. Energy resolution is the result of

statistical variations in the process of converting the incident photons into signal. Small

statistical variations in the photoelectron production efficiency, for example, have an

effect on the output signal (Knoll 2000).
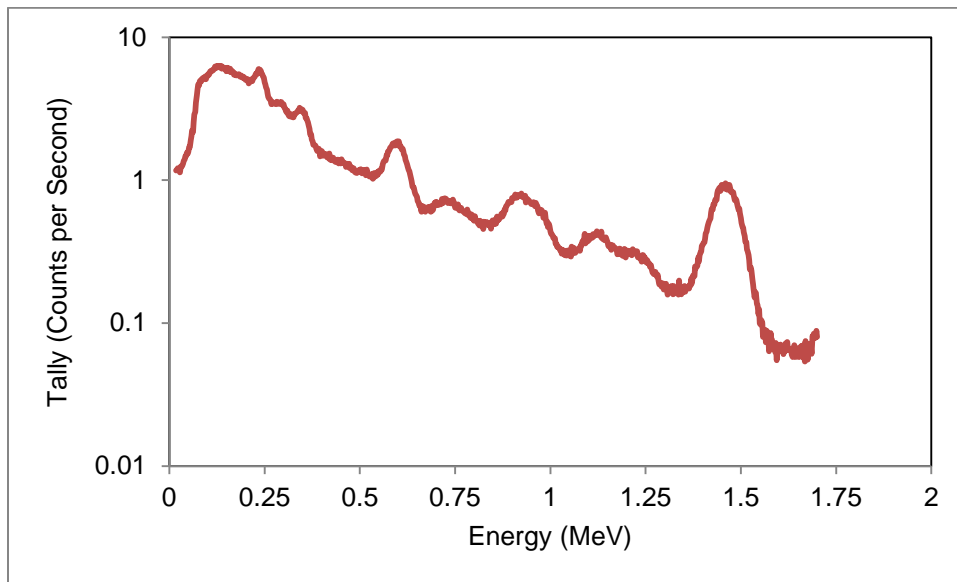
Fig. 2.3. MCNPX model of a typical concrete gamma ray background response in a
NaI(Tl) detector. The peaks are artificially broadened to simulate the statistical
resolution of a physical detector.

If two photon signals close in energy are measured with a detector with poor

resolution, the two peaks cannot be resolved. Properly functioning NaI(Tl) detectors

with modern electronics typically have a resolution of 6-7% at 662 keV and 20.0-23.3%

at 60 keV (Knoll 2000). This means that the $K_{\alpha1}$ and $K_{\alpha2}$ x rays listed in Table 2.1 cannot be resolved by the NaI(Tl) detector and will appear as one peak.

The pulse height spectrum for physical NaI(Tl) detectors also shows some small but important nonlinearities with photon energy. The scintillation efficiency of the NaI(Tl) crystal varies slightly with incident photon energy. This effect is dealt with in physical detectors by calibrating peak positions using sources with known gamma energies, usually including at least one high energy (1-2 MeV) and one low energy (<500 keV) peak.

Additionally, the electronic gain in NaI(Tl) detectors is somewhat sensitive to changes in temperature and applied electric field. The gain may drift over several hours during a long measurement or set of measurements. Electronic gain stabilization methods often minimize this effect by deriving an error signal from one or two isolated spectral peaks and making slight gain adjustments to keep the signal in the same channel (Knoll 2000). The calibration source that is the subject of this work is intended to serve as a calibration source, and if possible, a gain stabilization source, for a field NaI(Tl) instrument.

3. MONTE CARLO MODELING

Radiation emission and interaction with matter are both statistical processes. The Monte Carlo method is a statistical approach that models the behavior of individual radiation particles through their entire history using libraries of cross-section data for every known interaction. These cross sections are randomly sampled to determine the distance to an interaction, the type of interaction that will occur, the energy transferred to the model medium, the new direction of the incident particle, the distance to its next interaction, and the new direction and distance to interaction of any secondary particle produced in the interaction.

3.1.   MCNPX Transport Code

The Monte Carlo N-Particle eXtended transport code (MCNPX), version 2.6.0 was used to model ^{40}K radioactive emissions, interactions of those emitted particles in nearby materials, and the spectral characteristics in a model sodium iodide detector. MCNPX is a general purpose transport code that can be used for tracking of many types of interactions, from neutron, electron, photon, and any coupling of the three, to exotic particles like muons and pions. It can also track particles produced from interactions in materials, such as bremsstrahlung, delta (δ) rays, and K-edge characteristic x rays. MCNPX is available from the Radiation Safety Information Computing Center (RSICC) at the Oak Ridge National Laboratory (ORNL).

The main advantage of the MCNP method is that very complex, three-dimensional geometries can be modeled. Deterministic methods are limited by the

ability to express the system mathematically or by the data available. By tracking a large number of statistical particles, the MCNP code can deliver very precise results. MCNP also allows for the use of various variance reduction techniques in order to decrease computational time or reduce relative errors.

MCNPX was the code of choice for this project because of its ability to model distributed sources, interactions and secondary particle production in a complex geometry, and particle tallies that can simulate the output of a spectroscopic instrument.

3.2.   Detector Model

The NaI(Tl) detector was modeled based on a mechanical drawing from Sandia National Laboratory. The NaI(Tl) crystal itself measured 5.08 cm x 10.16 cm x 40.64 cm (2 in x 4 in x 16 in). The density of the crystal was 3.667 g cm^{-3}. The thallium dopant was considered insignificant and was not modeled (McConn et al. 2011).

The NaI(Tl) crystal was surrounded by a stainless steel detector casing 5.72 cm x 10.80 cm x 42.86 cm (2.25 in x 4.25 in x 16.875 in) and 0.10 cm (0.04 in) thick. Since the grade of stainless steel was not specified, 304L was arbitrarily chosen. The chemical composition for the modeled detector casing is shown in Table 3.1 (McConn et al. 2011). The steel had a density of 8.00 g cm^{-3}. The balance of the detector casing was filled with PTFE, better known by its trade name Teflon®. PTFE has the chemical formula C_2F_4 and was modeled with a density of 2.25 g cm^{-3}. The detector electronics were not modeled.

Table 3.1. Stainless steel 304L composition used for modeled detector casing.

Element	Mass %
C	0.030
N	0.010
Si	0.750
P	0.045
Cr	19.000
Mn	2.000
Fe	68.045
Ni	10.000

The detector and calibration source models are pictured in Fig. 3.1. The green object is the NaI(Tl) crystal itself, the stainless steel and PTFE are colored black, and a KBM calibration source is colored orange.
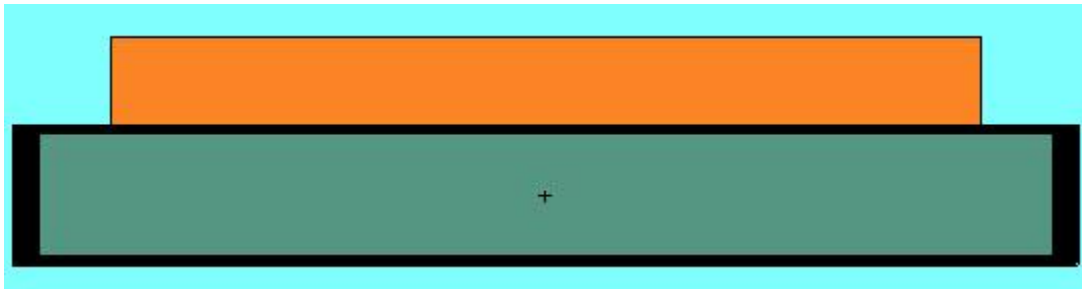
Fig. 3.1. XZ view of detector model with KCl-bismuth source.

3.3. Source Models

The calibration source was modeled as a rectangular prism 35.0 cm x 8.81 cm (13.4 in x 3.47 in) that covered 75% of the area of the detector crystal's top face. The length and width of the source was kept constant, but the thickness (and thus, total mass) of the source was variable. The source was composed of a homogeneous mixture of

potassium chloride (KCl) salt and ethyl carbamate (more commonly referred to as urethane, $C_3H_7NO_2$).

Two variants of this calibration source were tested. The first, the HZL method, interposed a thin foil of high-Z metal between the calibration source and the detector. This foil had length and width dimensions equivalent to those of the source matrix and a variable thickness. The second, the KBM method, added a homogeneous mixture of bismuth metal powder to the calibration source. The relative concentrations of all three constituents, as well as the source matrix thickness, were varied to determine their effect on the detector response. The calibration source modeling is described in more detail in Sections 4 and 5.

3.4. Model Source Term

While MCNPX can run coupled particle problems such as tracking the δ rays and K-shell x rays from a primary photon, it cannot track two primary particles in the same run. The gamma and beta emissions from the modeled ^{40}K sources thus were modeled in separate coding runs and summed in post-production using Microsoft® Excel® 2010.

While the source card for the gamma source required only the photon energy, the beta emissions required a more complex approach. Since beta emissions are stochastic, the modeled beta emission must be a distribution in energy and probability. The beta source cards used for this work are based on the work of Eckerman et al. (1994). They are openly available from the RAdiation Dose Assessment Resource (RADAR). The

modeled MCNP spectrum used is pictured in Fig. 3.2. The tabulated energy distribution

option *A* was selected (Shultis 2011).
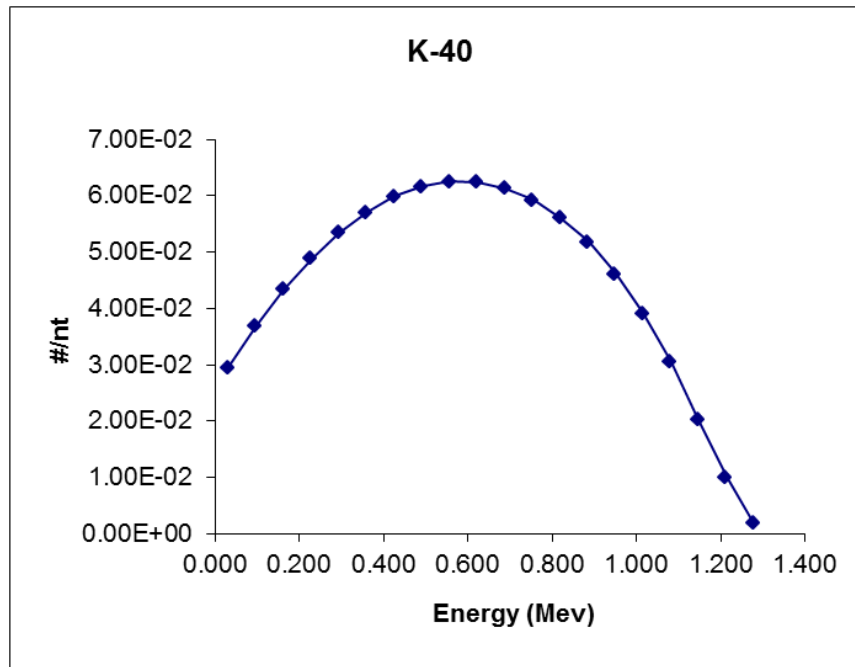
Fig. 3.2. Beta spectrum used in this work, available online at Radiation Dose Assessment Resource.

3.5. MCNPX Tallies

Tally cards are used to provide the user with information on the system. The

default tally options include particle flux across a surface or cell, flux at a point or ring,

energy deposition averaged over a cell, or the energy distribution of pulses created in a

detector, to name a few. The user may further divide these tallies into "bins" of cosine,

energy, or time, to obtain more detailed information on the particle behavior. These bins

may be subdivided further into smaller cosine, energy, or time bins.

MCNPX tallies are normalized to be per source particle by default, unless otherwise noted. The user must then renormalize the tally to the desired normalization, using either an FM multiplier card or a post-processing tool like Microsoft® Excel®.

3.5.1. Pulse Height Tallies

The F8 pulse height tally card was used to model the energy distribution of pulses in the NaI(Tl) crystal. The F8 tally works by summing the scoring tracks in a cell together into one value of energy deposited rather than tallying each scoring track individually. In this manner, its functions closely model real-world detectors, which record particles very closely correlated in time as one event (Pelowitz 2008).

The F8 tally allows for the modeling of the intrinsic statistical resolution of NaI(Tl) detectors using the Gaussian Energy Broadening (GEB) card. The GEB card uses the formula:

$$FWHM = a + b\sqrt{E + cE^2}$$ (3.1)

where E is the energy of the particle being measured, and a, b, and c are parameters input by the user. The (a, b, c) parameters used for this work were -0.00789, 0.06769, and 0.21159, respectively (Hakimabad 2007). The GEB card uses this function to sample a Gaussian function with the specified FWHM before scoring the particle (Pelowitz 2008). The FWHM of the NaI(Tl) detector crystal at the various energies of interest was calculated using this formula and is shown in Table 3.2.

Table 3.2. Calculated energy resolution and 99% bin width for NaI(Tl) detector at photon energies of interest.

Material	Z	Photon Energy (keV)	FWHM (keV)	FWHM (%)	99% bin width (keV)
Ta	73	57.535	8.44	14.7%	18.23
W	74	59.318	8.70	14.7%	18.78
Au	79	68.806	9.99	14.5%	21.58
Pb	82	74.969	10.79	14.4%	23.30
Bi	83	77.107	11.06	14.3%	23.88
^{40}K	19	1460.822	85.72	5.9%	185.06

Two separate F8-type pulse height tallies, numbered F8 and F18, were used to produce the x ray peak and pulse-height spectral data in Sections 4 and 5. The F8 tally used 2 keV energy bins to produce an output spectrum that strongly resembles a net spectrum (i.e. a measurement spectrum with the background subtracted). The bin widths of the second tally, F18, were chosen so as to obtain the total particles tallied in the x ray peak. Assuming that each peak is approximated by a Gaussian distribution, the FWHM can be related to the standard deviation of the Gaussian by

$$FWHM = 2\sigma\sqrt{2ln2} \approx 2.35\sigma \qquad (3.2)$$

99% of the area under the two-tailed Gaussian distribution is within $\mu \pm 2.58\sigma$, where μ is the mean of the distribution (i.e. the photon energy).

$$Bin\ width\ (99\%\ peak\ area) = \frac{2(2.58\sigma)}{2.35\sigma} = \frac{2(2.58\sigma)}{FWHM} = 2.196 * FWHM \qquad (3.3)$$

The 99% peak bin widths were related to the FWHM in this way. The F18 energy bins were determined using these values, so that the output could determine the number of counts in the x ray peak bins to the 99% confidence level. The optimal bin widths for the modeled peak tallies for each photon of interest are also included in Table 3.2.

26

The F8-type tally outputs the number of scoring tracks in each bin normalized to the number of particles run. This normalized output value must be multiplied by a normalization factor to obtain an output that can be related to physical quantities. The normalization factor N was defined as

$$N = \frac{\lambda_{40_K}}{M(K)*N_{Avo}} * Abun.\left(^{40}K\right) * BR(\beta \ or \ \gamma) \tag{3.4}$$

where λ_{40_K} represents the decay constant of ^{40}K in s^{-1}, $M(K)$ is the molar mass of natural potassium, 39.0983 g mol^{-1}, N_{Avo} is Avogadro's number: 6.022x10^{23} atoms mol^{-1}, and BR is the branching ratio of the beta particle (89.28%) or the gamma ray (10.66%). The abundance of ^{40}K in natural potassium, 0.0117%, is also included in the calculation. The value of N$_\beta$ was 28.335 s^{-1} (g ^{nat}K)$^{-1}$, and the value of N$_\gamma$ was 3.383 s^{-1} (g ^{nat}K)$^{-1}$. N was used to obtain useful tally values by the equation

$$T_i(E) = F8 \ Tally \ Output * N * m(K) \tag{3.5}$$

where T_i is the normalized value for F8-type tally output i in energy bin E, and $m(K)$ is the mass of natural potassium in the calibration source. The mass value is taken from the MCNPX Print Table 60, which provides the atom density, gram density, volume, and mass of each symmetric cell in the output. Excel® was used to normalize each energy bin for each tally. Modeled background sources were normalized using a similar equation

$$B(E) = F8 \ Tally \ Output * A_{tot} \tag{3.6}$$

Where B is the normalized value for the F8-type tally output for the background source term in energy bin E, and A_{tot} is the total activity of the source in Bq (s^{-1}). Throughout

27

this work, normalized F8-type tally values are represented as Tally (Normalized Unit). The normalized unit is usually counts s^{-1}.

Both normalized F8-type tallies have units of counts s^{-1}, which is a useful unit for radiation detection applications. This normalized output, however, does not necessarily accurately simulate real-world detector responses. When resources are available, each problem must be validated against experimental measurements to ensure that the simulation results accurately reflect real-world detector responses.

MCNPX tallies also include the relative error of each selected energy bin or summed tally value as part of the tally's output. The statistical variation corresponding to each value of T_i was given by

$$\sigma_{i_T}(E) = \eta(E)T_i(E) \tag{3.7}$$

Where σ_{i_T} is the standard deviation of T_i for energy bin E, and $\eta(E)$ is the relative error for energy bin E.

3.5.2. Dose Tallies and Procedure

Several tallies were used to determine the dose rates in air spheres at 0.1 cm (essentially a contact measurement) and 30.48 cm (1 foot) in terms of dose to tissue. The F5 point detector tally was used to evaluate the dose from source photons and secondary photons (x rays) produced from source electrons, and the F6 and *F8 tallies was used to evaluate the dose from source electrons.

The F5 point detector tally was used to determine the flux at points orthogonal to the top face of the calibration source, where the dose would be greatest. The flux was measured in air at several distances and converted into a dose in tissue using the dose

28

function (DF) card. The F5 radius of exclusion was 1.0 cm for each measurement point except for 1 mm, where the radius was 0.05 cm in order to avoid the calibration source material boundary. The ANSI/ANS-6.1.1-1991 Anterior-Posterior (AP) dose function (ic=31) was used to convert the flux values into those of dose for a human chest model with the radiation entering the anterior side. This method was used to determine the photon dose profile for both the beta and gamma source particles.

The electron dose profile in air was evaluated by measuring the energy deposition in air sphere cells. Air spheres were chosen in place of water spheres to avoid the irregularities that appear near material boundaries. The spheres had various radii in order to keep their cells from overlapping. They were placed at various intervals orthogonally to the top face of the calibration source (see Table 3.3). The unusually large detection spheres were selected because of the electrons' range in air (on the order of 10 cm for 100-keV electrons), and to improve the Monte Carlo statistics. Even if the spheres are large enough to appreciably disturb charged particle equilibrium, the result would be a conservative estimate of the air dose.

The energy deposition in these detector cells was measured using the F6 tally, whose output is normalized to MeV g^{-1}. The *F8 energy deposition tally results (with units of MeV) divided by the mass of the tally cells were used as a check for the F6 tally (Jung 2007). If the problem geometry was correct, the F6 and *F8 tally results and uncertainties were identical.

Table 3.3. Distances and radii of spherical air cells used to determine electron dose profile.

Source-Detector Distance (cm)	Detector Radius (cm)
0.10	0.05
1.00	0.5
2.54	1.0
5.08	1.0
10.16	1.0
15.24	1.0
22.86	1.0
30.48	1.0
45.72	1.0
60.96	1.0
100.0	1.0

The dose determination calculations required the renormalization of the MCNPX output data. The F5 tally output (units of Sv hr^{-1} source particle^{-1}) was renormalized using Equation 3.5, and its standard deviation was calculated using Equation 3.7. The final F5 tally data had units of Sv hr^{-1}.

The F6 tally output was in units of MeV g^{-1}. This was converted using Microsoft® Excel® to units of absorbed dose J kg^{-1} (gray). This value of absorbed dose was multiplied by the radiation weighting factors for electrons and photons to determine equivalent dose

$$H_T = w_R D_R \qquad (3.8)$$

The radiation weighting factors for both photons and electrons are unity, so in this case, the absorbed dose and the equivalent dose have equal values (ICRP 2007). The F8 tally was normalized in the same manner, with the additional step of dividing the tally output by the detector cell mass.

The F6 and *F8 tallies determine the dose delivered to the air medium. This calculated dose in air must be converted to a dose in tissue to match the tissue doses calculated by the F5 tallies for the gammas and x rays. The formula for converting dose in air to dose in tissue is

$$D_{tissue} = D_{air} \frac{\left(\frac{\mu en}{\rho}\right)_{tissue}}{\left(\frac{\mu en}{\rho}\right)_{air}} = D_{air} * \frac{0.0294\frac{cm^2}{g}}{0.0268\frac{cm^2}{g}} \qquad (3.9)$$

Where $\mu_{en}\,\rho^{-1}$ is the mass energy absorption coefficient for the medium.

The electron current exiting the top face of the source was determined using the F1 surface current tally. The tally output was broken into two directional bins using the cosine C card. The C card measures the direction of the tallied particles at their point of entry with respect to the positive normal to the surface (Pelowitz 2008). The net current was defined as the tally result of electrons exiting the source (cosine 0 to 1 in this case) subtracted by the tally result of electrons entering the source (-1 to 0).

3.6.   Variance Reduction

MCNPX includes several variance reduction techniques that can potentially decrease the computational time and the relative error of tallies. One of these techniques is known as importance sampling or geometric splitting. In shielding problems involving relatively weak sources or relatively powerful shields, often only a small number of the particle histories will pass through the shield to interact with the detector, leading to a large relative error. Importance sampling allows the user to split the shield into several separate cells, usually one mean free path of the particle in question, and assign each

31

successive cell a higher importance. When a particle encounters the boundary of a cell of higher importance, it is split into two particles, each with one-half the weight of the original particle, and each is tracked until it is captured or escapes the system. In this way, more particles may by tallied and thus reduce the associated relative error, but given that their weight is reduced, the tally returns the same result as without importance sampling (Pelowitz 2008).

However, importance sampling must be used with caution. In a self-shielding source, importance splitting can lead to much longer computational times. Particles that start their histories in the highest-importance cell immediately are split into 2^n particles, where n is the importance assigned to the cell. Each particle must be tracked until it is captured or escapes. When the source consists of 10 or more cells, each with an escalating importance, the computational time needed for each run becomes very long.

Importance sampling was used early in this work to split the source into cells with thicknesses of one x-ray mean free path or one electron range. However, as more cells were added, the computational times for 1e8 runs stretched to more than 48 hours each. Removing the importance sampling reduced the computational time to between 100 and 500 minutes per input, depending on the primary particle being tracked.

Source biasing is another common variance reduction technique. It involves the biasing the source sampling probability in order to improve the problem convergence rate. The weight of the source particles is adjusted to compensate so that the same tally result is reached with a reduced relative error. Note that the source biasing probability is separate from the true source sampling probability (SP card); altering the SP card would

alter the tally result. Source biasing was used in all simulations with a large concrete slab

source to obtain better statistics without altering the true source sampling probability

(Pelowitz 2008).

4.   SOURCE/TARGET DESIGN

4.1.   High-Z Layer Configuration

The HZL configuration consists of a KCl-urethane source matrix and a very thin high-Z target layer interposed between the source matrix and the detector. Particles from the source produce characteristic x rays through electron and photon interactions in the target. The ideal HZL calibration source design involves exploring the effects of four parameters on the overall x ray peak strength: 1) the source matrix dimensions, 2) the source matrix composition, 3) the high-Z target used for x ray production, and 4) the high-Z target's thickness. Other factors, such as physical size, mass, and materials costs were also considered. The ideal source matrix composition minimizes the concentration of urethane binding material, but the physical lower limit of concentration was not known. A value of 50 wt% KCl and 50 wt% urethane (overall density 1.5420 g cm^{-3}) was used for each HZL configuration. The dependence of the x ray peak strength within a three-dimensional parameter space is explored in this subsection.

The detector crystal's dimensions are 40.64 cm (16 in) long x 10.16 cm (4 in) wide, so the modeled source matrix's areal dimensions were arbitrarily set to 35.0 cm (13.8 in) long x 8.81 cm (3.5 in) wide. These dimensions covered 75% of detector crystal's area. The high-Z layer shared the source matrix's areal dimensions.

The remaining source matrix parameter to set in the model was its thickness. Thickening the source increases both the number of ^{40}K atoms present and the overall source activity. However, because of self-attenuation in the source, eventually a

saturation point is reached where adding more KCl matrix has virtually no effect on the

x ray signal. This concept of a saturation thickness is especially true for the short-ranged

beta particles.

The thickness of the KCl-urethane matrix was thus determined by the maximum

range of the ^{40}K beta particles. The source beta particles were modeled as a uniformly

distributed electron source with tabulated energies closely matching that of ^{40}K

(RADAR 2003). The empirical range-energy relation for beta particles devised by Katz

and Penfold (1952) is given by:

$$R_m = \begin{cases} 412E^{1.265-0.0954lnE} & ,0.01 \leq E \leq 2.5 \ MeV \\ 530E - 106 & ,2.5 \leq E \leq 20 \ MeV \end{cases} \tag{4.1}$$

where E = $KE_{\beta\pm}|_{max}$ for $\beta^{\pm}$ spectrum electrons. Using this empirical relation with the

1311.07 keV ^{40}K beta endpoint energy, a material-independent range of 0.5763 g cm^{-2}

was calculated. Dividing by the model source matrix density and neglecting range

straggling gives a maximum linear electron range of 0.3737 cm. This electron range was

used as the unit value of source matrix thickness in the 50/50 KCl-urethane mixture.

By defining the thickness of the KCl-urethane source matrix as a function of the

maximum electron range, the source thickness is dependent only on the matrix density.

The KCl-urethane matrix geometry can then be optimized without precise knowledge of

the material's chemical composition. The ranges of electrons in several KCl-bismuth

matrix densities are given in Table 4.1.

Table 4.1. Maximum range of [40]K beta particles in matrices of various densities.

KCl Matrix Density (g cm^{-3})	Maximum Electron Range (cm)
1.25	0.461
1.50	0.384
1.75	0.329
2.00	0.288
2.25	0.256
2.50	0.231
2.75	0.210
3.00	0.192

MCNPX was used to test the x ray response in the detector for source thicknesses up to 12 electron ranges. Since MCNPX can only use one input source particle at a time, the [40]K beta and gamma emissions were tested separately using the same geometry conditions. A 0.00371 cm gold layer (0.25 mean free paths of the 68.8 keV gold x ray) was selected to be interposed between the source and the detector for these thickness tests.

The results of MCNPX simulations to determine the optimal source matrix thickness are shown in Fig. 4.1. 1σ error bars are included for all data points, but they are obscured by the data symbols. The x ray peak's beta component begins to reach saturation near 10-12 electron ranges, but the magnitude of the x ray peak continues to increase virtually linearly. The mean free path of the 1460.8 keV gamma ray is 27.4 cm in the KCl-urethane matrix (Berger et al. 2010), so the upper bound of the source matrix thickness was bounded by practical weight limits and construction concerns. A source thickness of 10 electron ranges (3.737 cm) was selected to be used in exploring the characteristics of the high-Z layers.
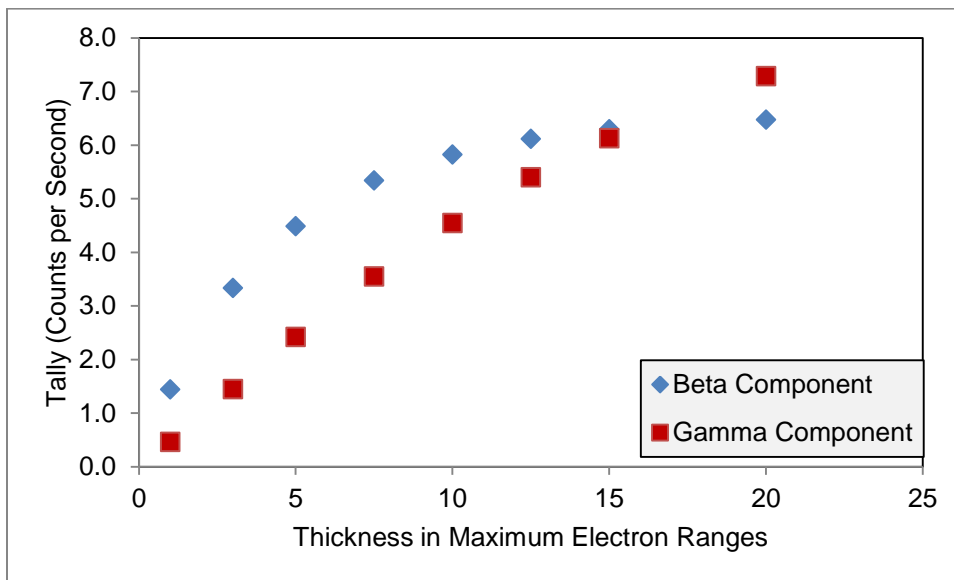
Fig. 4.1. A comparison of the relative contributions of the beta and gamma components to the simulated x ray peak using the high-Z layer method.

The thickness of four high-Z metals was varied to determine the effects on x ray peak strength. The four metals were tantalum (Ta), tungsten (W), gold (Au), and lead (Pb). Contrary to the KCl-urethane source matrix, the thickness of the high-Z layer was measured in units of the photon mean free path. The mass attenuation coefficients for the $K_{\alpha 1}$ x ray energy in each high-Z target material were determined by linear interpolation from the NIST X-ray Mass Attenuation Coefficient Tables (Hubbell et al. 2004). The mean free paths are listed in Table 4.2.

Table 4.2. Mean free paths for $K_{\alpha1}$ x ray in high-Z metals.

Material	Z	Density ρ (Attix) (g cm^{-3})	$K_{\alpha1}$ X Ray Energy (Firestone) (keV)	μ/ρ (NIST) (cm^2 g^{-1})	μ (cm^{-1})	mfp (cm)
Ta	73	16.65	57.535	4.098	68.24	0.01465
W	74	19.30	59.318	3.865	74.60	0.01340
Au	79	19.29	68.806	3.496	67.45	0.01483
Pb	82	11.33	74.969	3.074	34.82	0.02872

Several trends are apparent when the x ray production in the four metals is plotted in Fig. 4.2. First, in each case, the x ray response as a function of material mean free path appears to follow a sigmoidal curve that remains consistent across all four metals. Second, higher-Z targets produce a larger x ray signal in the detector. This is because the higher-Z metals (i.e. gold, lead) emit $K_{\alpha1}$ x rays with higher energies than the lower-Z metals (i.e. tantalum, tungsten). This x ray is more penetrating and thus less likely to be attenuated before reaching the NaI(Tl) crystal.

Fig. 4.3 shows that the sigmoidal curve is a result of the relative contributions of the two types of particles emitted by ^{40}K. Below 1.5 mean free paths, the contribution of the source beta particles increases rapidly as the layer thickness decreases. Simultaneously, the gamma contribution decreases below one mean free path as fewer 1460.8 keV gamma rays interact with the target metal. This is because the 1460.8 keV gamma ray has a relatively long mean free path, and because gamma rays produce x rays less efficiently than beta particles due to the extra step of creating δ-rays. Reducing the layer thickness thus reduces the volume for potential gamma interactions. Both source particles appear to reach equilibrium as the metal thickness increases. Lead is shown as

an illustrative example in Fig. 4.3, but this component-specific response is replicated in each of the four materials.
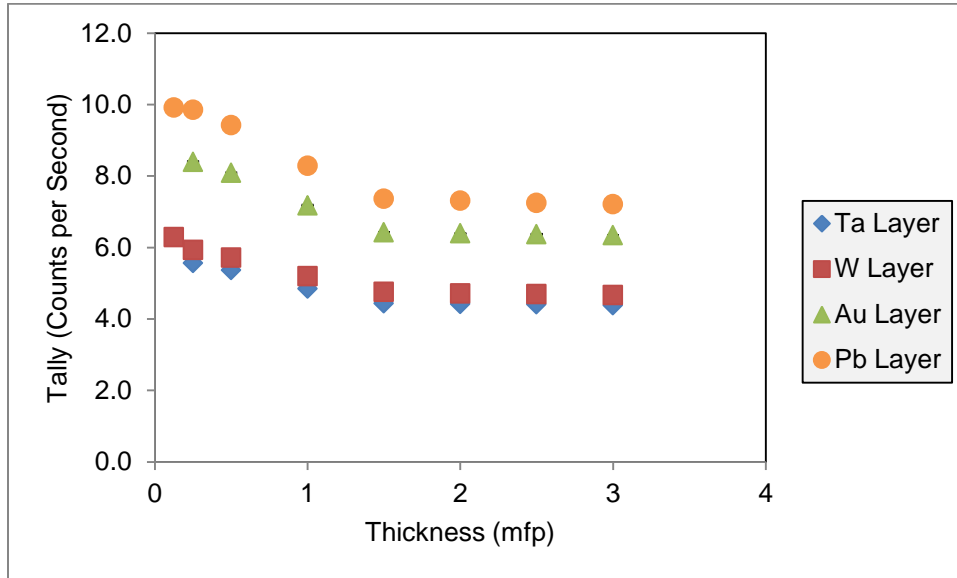
Fig. 4.2. Comparison of simulated x ray production in high-Z layer materials, as a function of mean free path thickness.
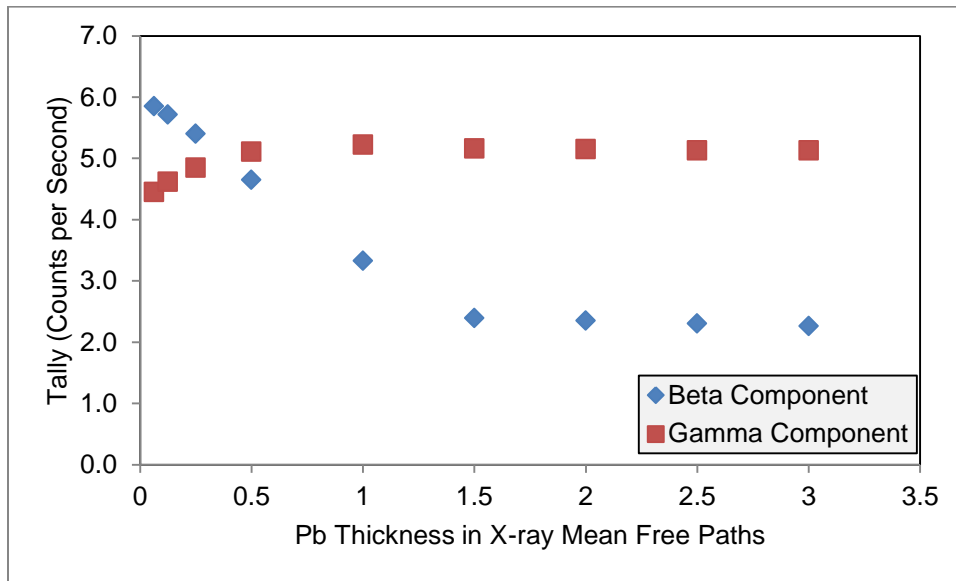
Fig. 4.3. Beta and gamma components of the simulated x ray peak strength in lead, as a function of mean free path thickness.

Mean free path was used for convenience in modeling, but as seen in Table 4.2, each metal has a different mean free path due to their differences in density, mass attenuation coefficient, and x ray energy. The density thickness is a unit of measure used to compare photon attenuation in materials of differing densities. The x ray response as a function of density thickness is shown in Fig. 4.4.
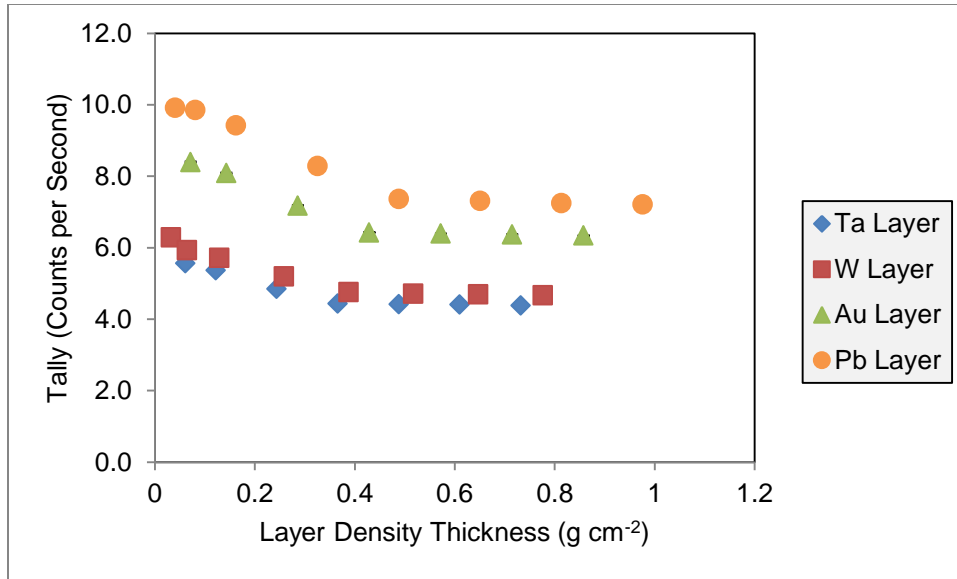
Fig. 4.4. Comparison of x ray response in high-Z layer metals, as a function of density thickness.

The optimal x ray peak response in high-Z layer simulations used 0.25 mean free paths of lead (0.00718 cm). However, since bare lead is considered to be a hazardous material, 0.25 mean free paths of gold (0.00371 cm) is used as the model high-Z layer geometry throughout the rest of this work.

4.2.   Bismuth Matrix Configuration

The KBM configuration consisted of bismuth metal powder mixed homogeneously into a KCl-bismuth-urethane matrix. Unlike the HZL method described in Section 4.1, the KBM produces x rays in the same medium as the primary particles. However, the same principles that guide the optimization of the KCl-urethane source matrix hold here. The x ray peak strength depended on the relative values of four parameters: 1) the concentration of KCl in the matrix, 2) the concentration of bismuth, 3)

the concentration of urethane, and 4) the source dimensions. The areal dimensions of the source were set equal to those of the HZL configuration, so only the variance in the KBM thickness was explored. As with the HZL configuration, the physical size, mass, and materials costs were also taken into account.

The KBM thickness was the first parameter tested. The KBM thickness was defined in terms of the 77.107 keV $K_{\alpha 1}$ bismuth x ray mean free path. Defining the matrix thickness in terms of mean free path removes the dependence on material composition and makes the source thickness dependent only on the density.

The reference source/target matrix for determining the optimal source thickness was modeled as a homogeneous mixture of 50 wt% KCl, 45% wt% urethane, and 5 wt% bismuth. The reference model's density was 1.9735 g cm^{-3}. For this reference matrix, the beta component begins to reach saturation near 15 x ray mean free paths (see Fig. 4.5), while the gamma component increases in a nearly-linear fashion.
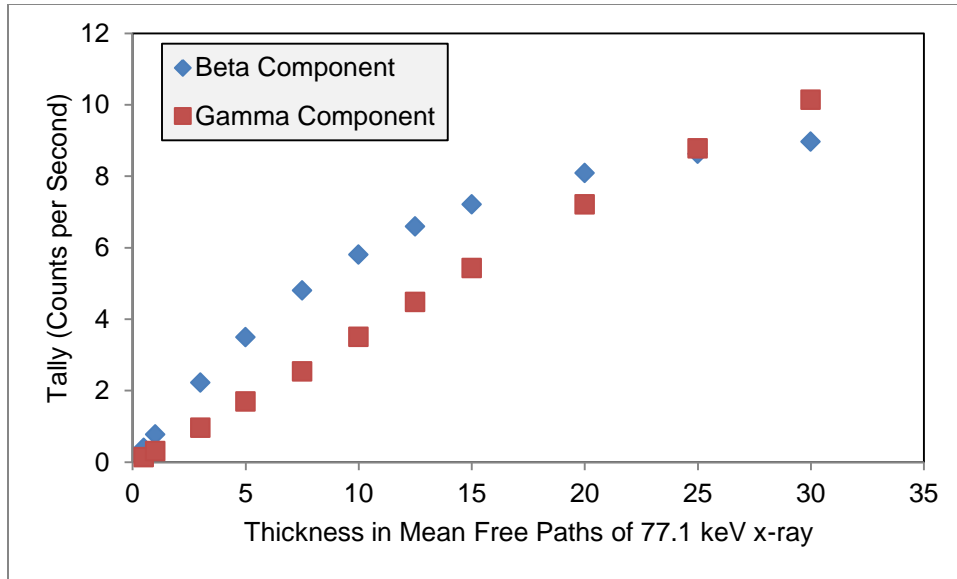
Fig. 4.5. Comparison of the beta and gamma components to the x ray peak in KCl-bismuth reference geometry.

Using a set KBM thickness of ten mean free paths, the x ray peak response was modeled as a function of material composition. Three sets of material compositions were tested in MCNPX: 30 wt% urethane, 50 wt% urethane, and 70 wt% urethane. The bismuth concentrations in each set were varied between 0.5 wt% and 15 wt%. The KCl concentration was the balance of the material in the matrix. Urethane concentration was held constant to determine the effects of varying the bismuth-potassium ratio; if the KCl concentration were held constant while those of bismuth and urethane were varied, the x ray response would increase until reaching a saturation plateau where variances in the bismuth concentration would have a negligible effect on x ray peak strength.

The relative x ray peak strengths of the three KBMs with constant urethane concentrations are shown in Fig. 4.6. For each urethane concentration, a plateau region is visible where the x ray peak strength remains constant within ±2% for a range of

43

bismuth concentrations. On either side of this plateau, the x ray response decreases due to either incomplete utilization of source particles or too few source particle emissions from ^{40}K.
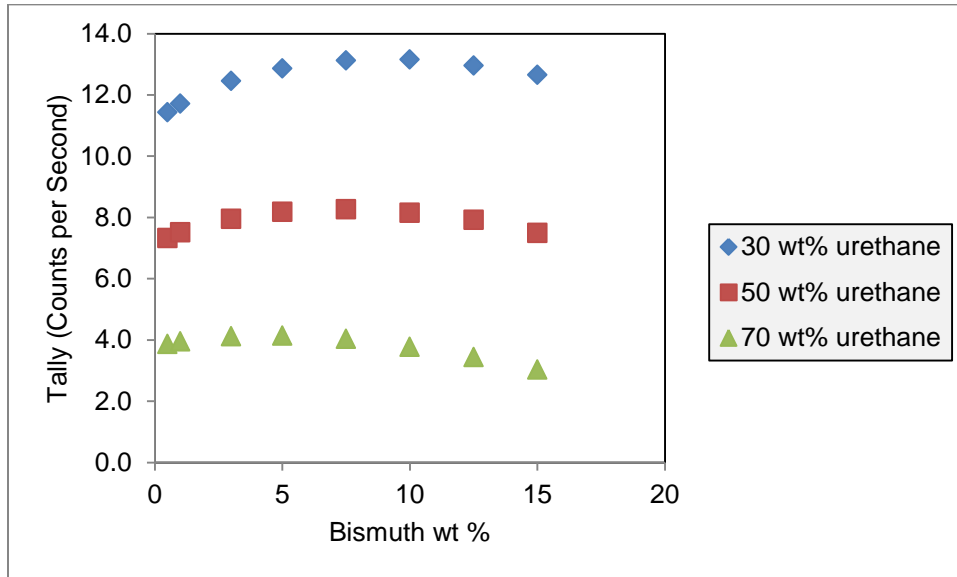
Fig. 4.6. X ray peak response as a function of bismuth concentration for three different urethane compositions.

Plotting the x ray peak response as a function of the bismuth-potassium mass ratio (Fig. 4.7) shows that the plateau region occurs when the bismuth-potassium ratio is between 0.1 and 0.2, regardless of the urethane concentration. Based on these results, the 46 wt% KCl-4 wt% bismuth matrix (mass ratio 0.166) will be used as the development model throughout the remainder of this work.
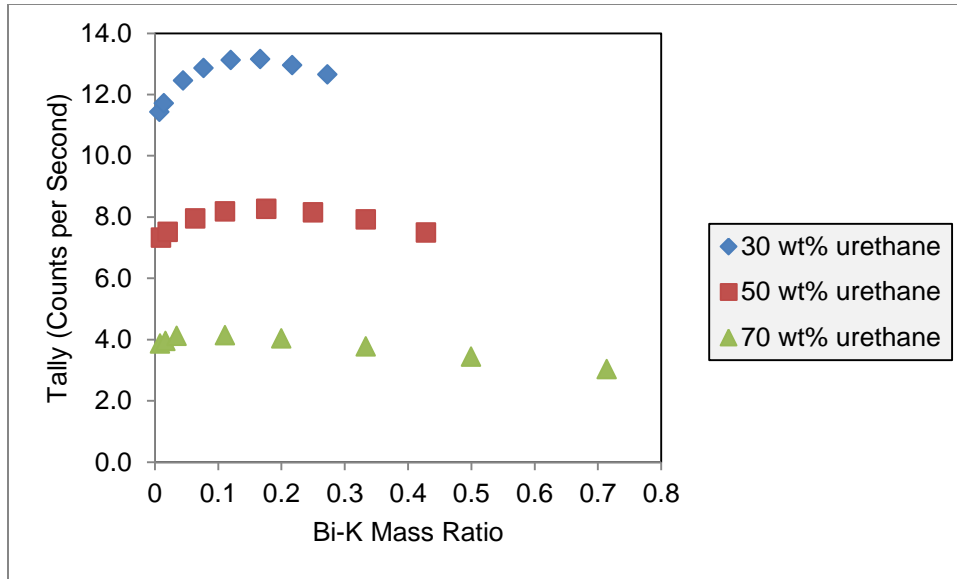
Fig. 4.7. X ray peak strength as a function of bismuth-potassium mass ratio.

5.   RESULTS AND DISCUSSION

5.1.   Comparison of High-Z Layer and KCl-Bismuth Matrix Methods

5.1.1.   Configuration Comparison Using Source Thickness

Though the two calibration source configurations share the same basic approach to producing x rays (inducing K-shell fluorescence in a high-Z material), they differ in their construction and methods of delivering x rays to the detector.

Fig. 5.1 shows a comparison of the two methods' x ray peak strengths as a function of the mass of potassium in the source. The HZL configuration shown used a 50/50 KCl-urethane source matrix with a 0.25 mfp thick (0.0037 cm) gold layer, and the KBM configuration used a homogenous matrix consisting of 4 wt% bismuth, 46 wt% KCl, and 50 wt% urethane. The two curves match closely until about 200 g potassium, until the KBM configuration begins to display a stronger x ray peak. This difference is likely due to the KBM configuration's and smaller average distance between the radioactive potassium atoms and the bismuth atoms. The KBM matrix is also more dense than the HZL's source matrix, which makes the KBM matrix thinner and reduces the distance the source particles must travel to produce x rays, and the distance the x rays must travel to produce signal in the detector.
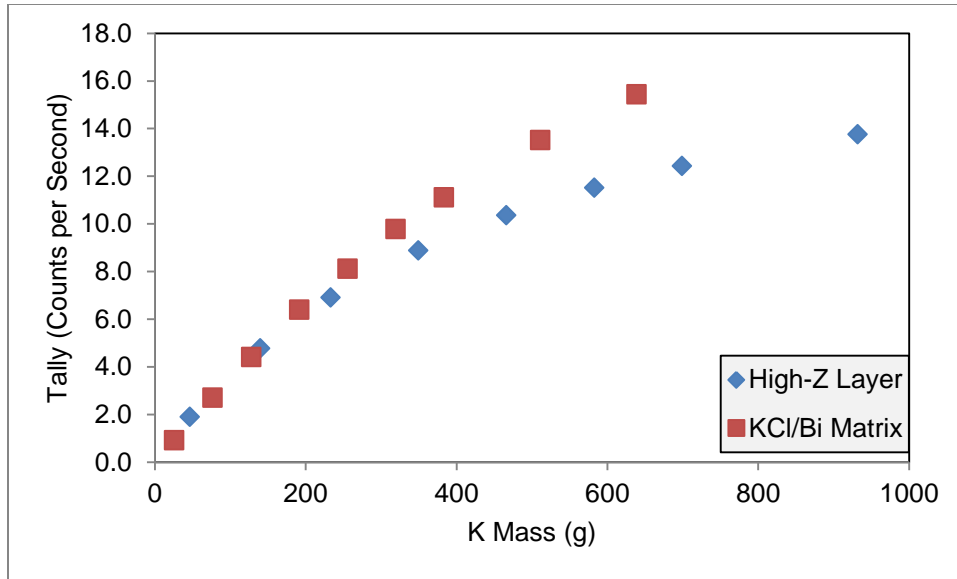
Fig. 5.1. Comparison of x ray peak strength as a function of potassium mass used for the two x ray production methods.

5.1.2.   *Configuration Comparison Using Model Pulse-Height Spectra*

The two configurations were compared using identical amounts of KCl source material in Fig. 5.2. Each calibration source used 466 g of natural potassium (54.5 mg of ^{40}K). The HZL configuration was modeled as 0.25 mean free paths (0.037 mm) of gold with a 50 wt% KCl-50 wt% urethane matrix. The simulated KBM configuration used 77.3 g of bismuth powder (4 wt%).

Using identical amounts of ^{40}K, the KCl-bismuth matrix collected 12.7 ± 0.03 counts per second in its x ray peak, while the gold layer collected 8.71 ± 0.02 counts per second. This difference could be due to the reduced distance the ^{40}K emissions must travel in the KBM configuration to produce x rays, and the fact that 77.1 keV x rays are slightly more penetrating than 68.8 keV x rays.

Fig. 5.2b shows a detail view of the x ray peaks, bremsstrahlung continuum, and Compton backscatter peak from the 1460.8 keV gamma ray for each configuration. The bismuth-induced x ray peak stands much further above the Compton continuum than the gold-induced x ray peak. This separation from the Compton continuum is essential for using this source in an unshielded environment with natural background.

The beta and gamma contributions to each x ray peak are shown in Fig. 5.3. The bismuth-induced x ray peak stands more prominently above both the bremsstrahlung continuum (~110-250 keV in beta component) and the Compton continuum (photon spectrum) than the gold-induced x ray peak. The importance of maximizing the beta contribution is apparent, as even in the KCl-bismuth matrix, the Compton backscatter peak creates a greater response in the detector than the gamma induced x rays.
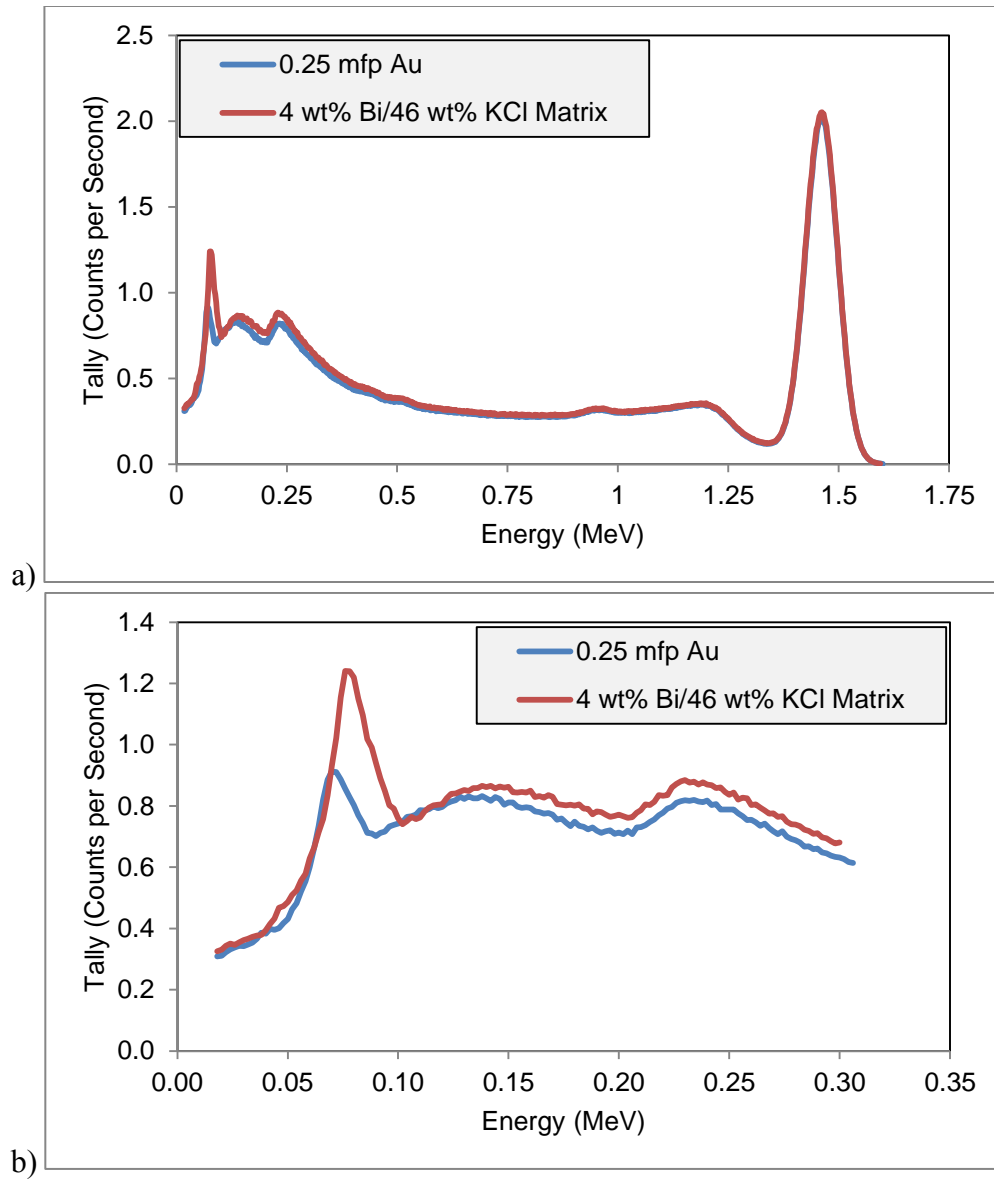
Fig. 5.2. Comparison of 0.25 mfp gold HZL and 4 wt% bismuth KBM configurations for
a) full spectrum and b) x ray region.
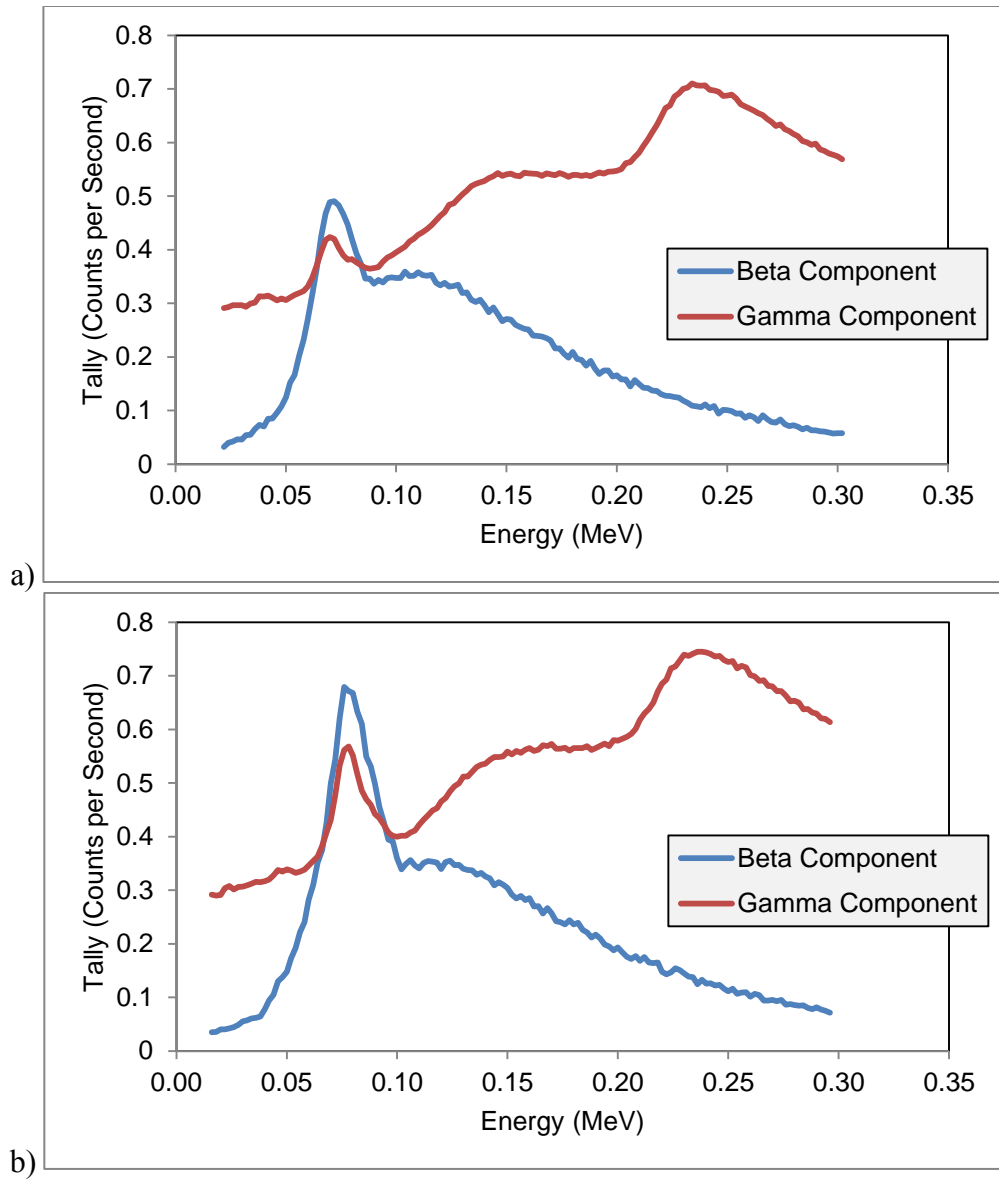
Fig. 5.3. Beta and gamma contributions to x ray peak in a) gold layer configuration and b) KCl-bismuth matrix configuration.

5.1.3. *Background Interference Comparison*

Physical gamma spectroscopy systems must be able to operate in the presence of the natural background. The decay products of primordial ^{238}U and ^{232}Th are the main contributors to the natural gamma ray background near sea level. Compton interactions in earth and building materials create a continuum of gamma rays across the spectrum that can obscure weak, low-energy peaks. Concrete and asphalt are both likely to be encountered in field operations. Both emit relatively strong gamma backgrounds due to their tendency to concentrate ^{40}K and primordial uranium and thorium. The work of Ryan (2011) was used to prepare a concrete disk 5.0 m in diameter and 10 cm thick, which emitted one of two different isotropic photon source terms, one with a very strong background (889 Bq kg^{-1}; 352 gammas kg^{-1} s^{-1}) and one relatively weak background (70.6 Bq kg^{-1}; 34.0 gammas kg^{-1} s^{-1}). The spectra from the two background decks are shown in Fig. 5.4. These background decks were used to model the HZL and KBM calibration sources in an open, outdoor environment (i.e. an open concrete pad), to determine the configuration least susceptible to background.
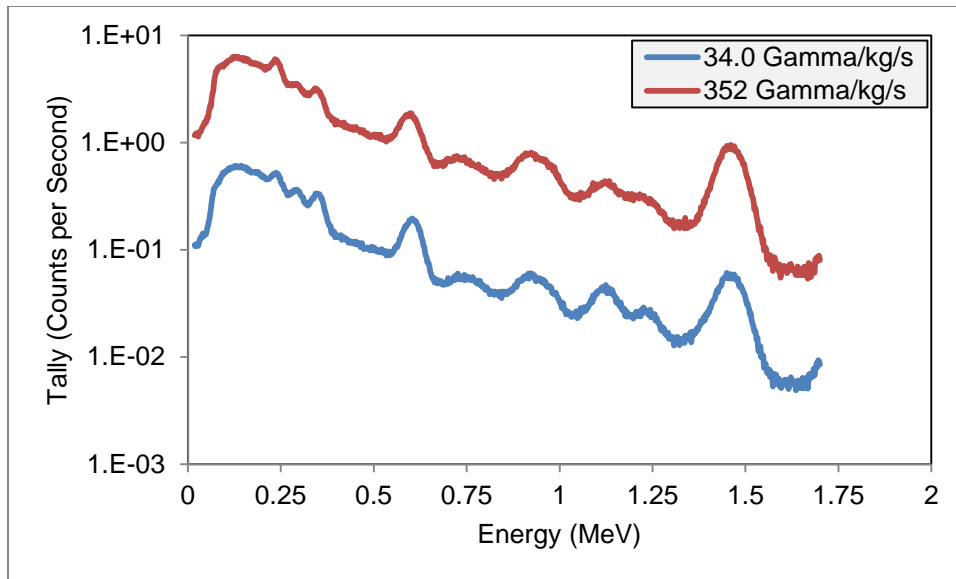
Fig. 5.4. Simulated pulse-height spectra for the two background decks used to test calibration source performance in presence of background.

The detector was placed in the center of this concrete disk, and the calibration sources were placed both on top of the detector (opposite the concrete) and between the detector and concrete, as pictured in Fig. 5.5. When the calibration source is oriented towards the largest source of background (usually the ground), it can serve as a shield for low-energy gamma rays as well as producing a small additional amount of fluorescence x rays. These model geometries were meant to determine if the calibration source location had a measureable impact on the x ray peak strength.

The simulated background spectra are shown without the calibration source contribution in Fig. 5.6. The calibration sources themselves provide up to a 30% reduction in the strong background photon spectrum below 300 keV. This shielding contributes to the x ray peak strength by suppressing the background. However, since the source is designed to be a permanent or semi-permanent fixture on the detector, the

52

background shielding signifies a reduction in sensitivity to low-energy and low-activity sources. The reduction in sensitivity is a factor that will be considered in more depth in Section 5.5.

Fig. 5.5. Calibration source geometry with source a) between and b) opposite the concrete background source.

Fig. 5.7 shows the calibration source and the weak background components to the simulated pulse-height spectrum. Both the HZL and the KBM sources create measurable peaks above the background and the bremsstrahlung and Compton continua. The main concern with the weak background source term is that the dramatic increase in overall count rate can obscure low-activity external sources, especially in the low-energy portion of the pulse-height spectrum.
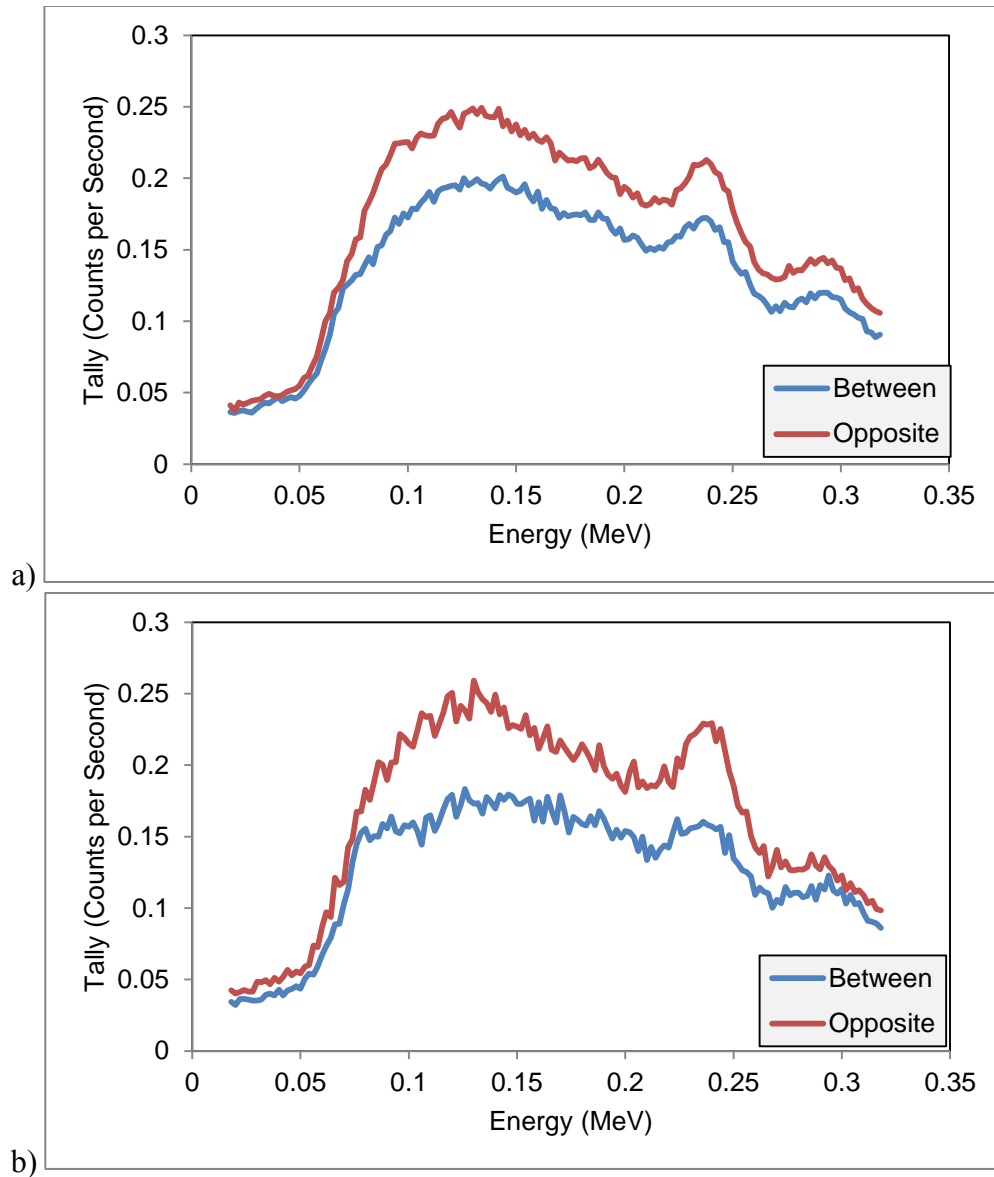
Fig. 5.6. X ray regions for strong model background (352 gammas kg^{-1} s^{-1}) without calibration source contribution for a) 0.25 mfp gold and b) 5 wt% bismuth.
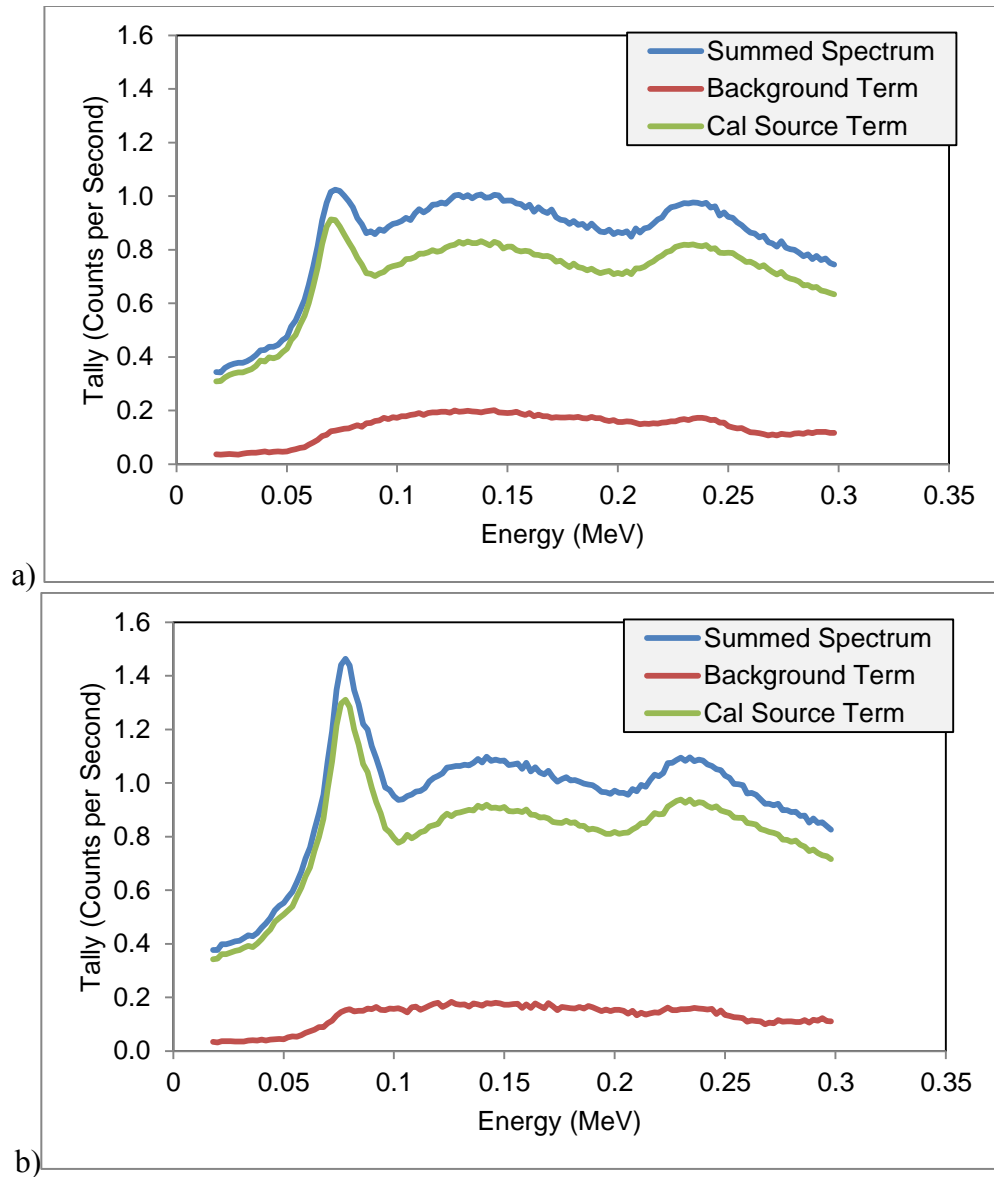
Fig. 5.7. Contributions to x ray region for a) 0.25 mfp gold and b) 4 wt% bismuth with weak model background (34.0 gammas kg^{-1} s^{-1}).

Fig. 5.8 shows the source contributions in the presence of a strong background source term (352 Bq kg^{-1}). In this case, both methods produced much less prominent x ray peaks above the background, even with the added advantage of orienting the calibration source towards the background source to take advantage of the shielding

55

effect. The KBM configuration shows an x ray peak that reaches approximately 0.5 count s^{-1} above the background continua at its most prominent.
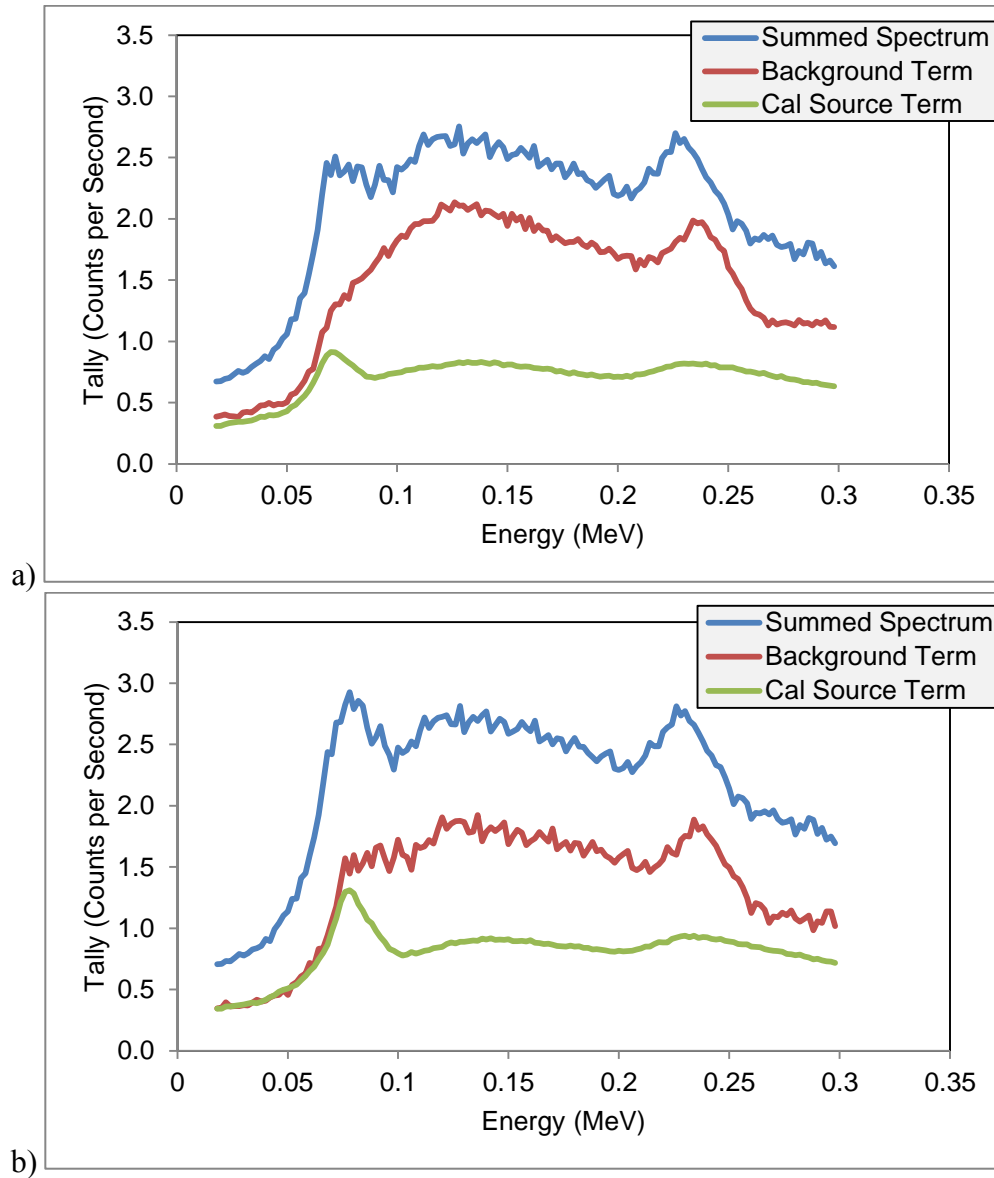
Fig. 5.8. Contributions to x ray region for a) 0.25 mfp gold and b) 4 wt% bismuth with strong model background (352 gammas kg^{-1} s^{-1}).

5.1.4. Materials Cost Comparison

In addition to performance factors, cost is another major consideration in the selection of the calibration source method. The estimated costs of the metals simulated in this work are shown in Table 5.1 (USGS 2011). The price for tantalum and tungsten is based on their oxide forms, which are traded on the commodities markets. Since the metal forms are desired for this application, an additional chemical conversion would be included in their overall cost. Tantalum, tungsten, gold, and lead would all require electroplating the metals onto the stainless steel surface of the detector, which would add an additional production cost. Bismuth powder would only require thorough mixing with KCl salt, which would incur only a minor production cost.

Table 5.1. Estimated 2011 prices for metals tested in this work.

Metal	Mass (g)	2011 Avg. Price[a]	2011 Avg. Price ($ g^{-1})	Metal Cost for One Source
Ta	18.80	130 \$/lb Ta_2O_5	\$0.29	\$5.39
W	19.94	250 \$/mtu WO_3	\$0.03	\$0.50
Au	22.08	1600 \$/oz	\$56.44	\$1,245.91
Pb	25.09	1.24 \$/lb	\$0.003	\$0.07
Bi	77.32	11.6 \$/lb	\$0.03	\$1.98

[a]All prices from United States Geological Survey (USGS) Commodity Statistics and Information

The bismuth-based calibration source would be the most economical in terms of cost and simulated performance, both with and without the inclusion of background source terms. For these reasons, only the bismuth-based calibration source is considered henceforth in this work.

5.2.   Maximizing Bismuth-Based Calibration Source Performance

The total number of counts accumulated in the x ray peak must exceed a

statistical threshold, usually less than 5% uncertainty. Assuming Poisson statistics, this

5% threshold is reached at 400 counts above continuum (CAC) in the x ray peak area.

The CAC is a value meant to separate the counts in the x ray peak and the counts in the

Compton continuum. Gamma spectroscopic analysis software packages use

sophisticated methods, including linear and exponential methods, to determine the CAC

(which is often called "net peak area"). MCNPX, however, is only capable of providing

the total number of counts in the energy bins of interest; any evaluation of the CAC must

be done in post-processing.

The linear method was used to determine the CAC in the x ray peaks. As shown

in Fig. 5.9, a line was drawn across the x ray peak, from 65 keV to 89 keV (the width of

the 99% confidence level). These two energies were used as the vertices of a trapezoid.

The area of the trapezoid was used to represent the number of tallies in the Compton

continuum, which was subtracted from the F18 tally output (the 99% peak bins) to

determine the CAC. The linear method does not appear to cover the entire peak because

of two different interferences. The first is the bismuth K_β x rays, which have higher

energies but lower probabilities of emission (the most probable is the $K_{\beta1}$ x ray, which

has an energy of 87.35 keV and is emitted 10.7 times for every 100 K shell vacancies,

4.5 times less frequent than the $K_{\alpha1}$ x ray. The second source of interference is a

background ~92.5 keV doublet gamma ray associated with ^{234}Th (absolute intensity

4.8%), a decay product of ^{238}U (Kaste et al. 2006). More advanced spectroscopic

software would not resolve this interference, but would instead perform the linear method from ~68-96 keV. This would likely result in a larger number of counts above continuum and thus a shorter time needed to reach 5% uncertainty in the x ray peak.
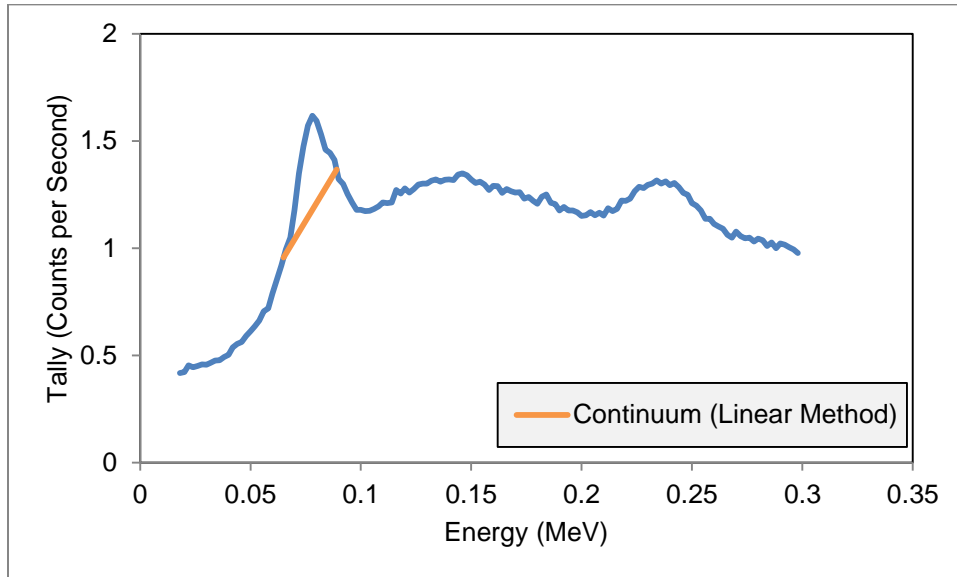
Fig. 5.9. The linear method was applied to the MCNP tally output to determine the counts above continuum.

While maximizing the x ray peak strength is the objective of these simulations, the detector sensitivity must also be considered. Adding more calibration source material eventually reaches a point of diminishing returns. Adding more calibration source material also adds to the total count rate and shielding effectiveness of the calibration source, both of which decrease the detector's sensitivity. The effects of these competing factors must be considered when selecting the development model.

Using a homogenous mixture of 46 wt% KCl and 4 wt% bismuth, the CAC and the time to collect 400 counts in the peak above continuum were calculated for source

matrices with various masses of natural potassium. The results are shown in Table 5.2 and Table 5.3. Note that all tabulated total count data represents the total counts above an 18 keV threshold.

The counts above continuum per second increase virtually linearly with increasing source matrix mass. The time needed to reach 5% uncertainty in the x ray peak decreases as more source material is added, but the amount of decrease begins to level off as the source approaches saturation. The difference between the times needed for the two source locations to reach 5% uncertainty decreases as more source material is added. This is because the calibration source term becomes more dominant over the background term with an increase in source material. Source location has no significant effect on the CAC at 500 g potassium or above. The strong background appears to collect more counts in the x ray peak than the weak background; this is because of a minor interference with the 92.5 keV gamma ray corresponding to that of ^{234}Th. The large overall effect of the background source term on the detector's x ray peak response illustrates the need for a well-characterized and mostly constant background during validation measurements.

The effect of the calibration source on the background is also apparent in Table 5.2 and Table 5.3. As the amount of material in the source increases, the calibration source begins to have a significant shielding effect on the background. The source is a less effective shield for higher background count rates. Placing the source away from the detector has no statistically significant effect, regardless of background count rate.

Table 5.2. Performance measures for calibration source with weak model background, calculated for several masses of potassium in source matrix.

Source Location	K Mass (g)	CAC (s^{-1})	CAC σ	Cal Source Total CPS	Cal Source Total CPS σ	% Bkg Change
Between	100	0.57	0.023	106	0.024	-6.77%
	250	1.53	0.029	237	0.044	-15.02%
	500	2.80	0.040	399	0.075	-24.11%
	750	3.67	0.050	511	0.100	-30.03%
	1000	4.18	0.058	590	0.205	-33.99%
Opposite	100	0.49	0.014	106	0.024	-0.99%
	250	1.45	0.023	237	0.044	-0.19%
	500	2.72	0.037	399	0.075	0.77%
	750	3.59	0.048	511	0.100	1.32%
	1000	4.10	0.056	590	0.205	1.63%

Table 5.3. Performance measures for calibration source with strong model background, calculated for several masses of potassium in source matrix.

Source Location	K Mass (g)	CAC (s^{-1})	CAC σ	Cal Source Total CPS	Cal Source Total CPS σ	% Bkg Change
Between	100	2.39	0.218	120	0.024	-6.06%
	250	3.54	0.207	265	0.055	-12.43%
	500	4.63	0.198	438	0.094	-18.82%
	750	5.55	0.194	556	0.176	-22.52%
	1000	5.56	0.194	639	0.205	-24.70%
Opposite	100	1.68	0.225	120	0.024	-0.94%
	250	2.81	0.227	265	0.055	-0.12%
	500	4.22	0.232	438	0.094	0.86%
	750	5.20	0.234	556	0.176	1.48%
	1000	5.79	0.235	639	0.205	1.83%

5.3.   Spectral Acquisition Simulations

The tables and spectra in Section 5.2 were calculated using simulations with

1×10^8 particle histories each for the beta and gamma source components. This number of

particle histories corresponds to approximately 7000 s of data from the source beta

particles and 59000 s of data from source gamma rays in a 500 g potassium source.

This calibration source is designed to be used in field operations, where counting

times are limited and this level of precision is virtually never reached. A set of MCNPX

runs were executed where the number of particle histories corresponded roughly to the

number of particles emitted in time span X for the source beta particles, source gamma

rays, and the background gamma rays. These three outputs were summed to simulate

pulse-height spectral acquisitions of 60, 300, 600, and 900 s in a physical detector in

order to determine if the x ray peak could be discerned by the operator and the computer

software.

Two acquisition simulations used with the 500 g potassium source and weak

background source term are shown in Fig. 5.10 and Fig. 5.11. Note that the ordinate has

been altered to show the total counts per channel rather than the count rate per channel,

and that a logarithmic scale was used. The 300 s simulation collected 1098 CAC in the x

ray peak, an average of 219.6 per minute. This peak is easily readable by gamma

spectroscopy software packages and would serve as a low-energy calibration point in

relatively weak background environments. However, the count rate is still too low to be

used as a gain stabilization source, especially in such a high-background area of the

spectrum.
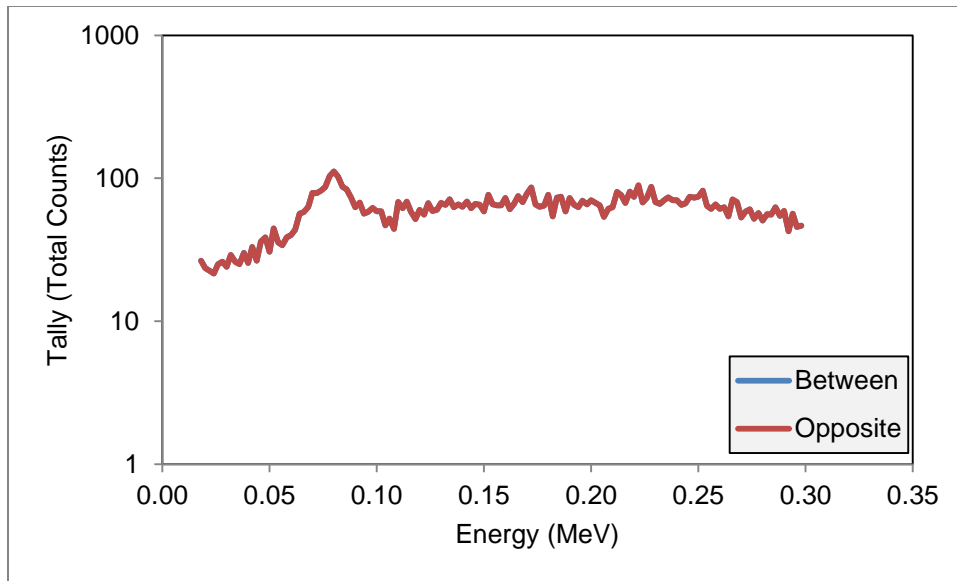
Fig. 5.10. Simulated 60 s spectral acquisition with 500 g potassium source and weak background source term.
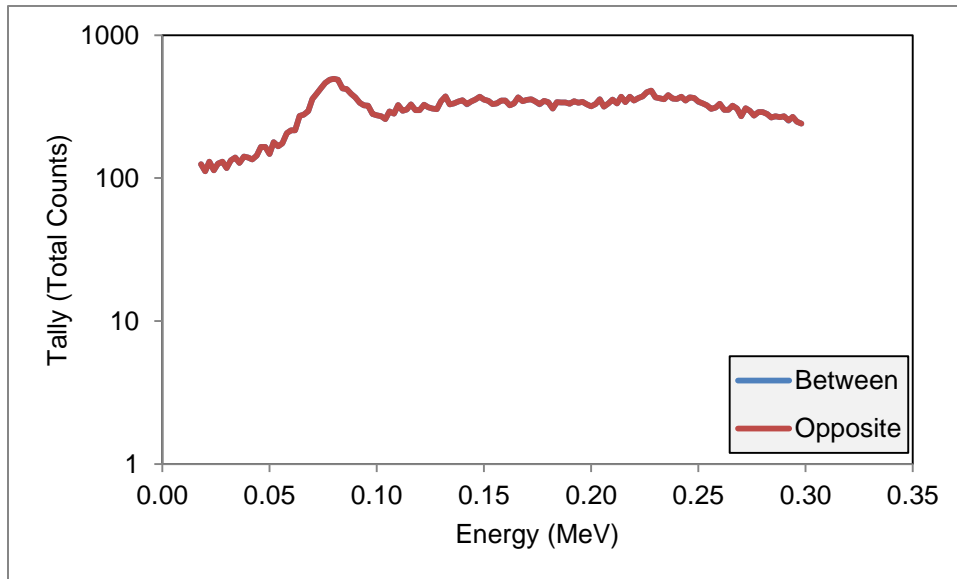
Fig. 5.11. Simulated 300 s spectral acquisition of 500 g potassium source and weak background source term.

The 500 g potassium source was also tested with the strong background source term in a series of acquisition simulations. The spectra from the 300 s and 600 s simulations are shown in Fig. 5.12 and Fig. 5.13. The x ray peak is more difficult to distinguish from background. Users would likely have to switch to a linear ordinate to discern the peak from the background continuum. The 300 s simulation collected 1268 CAC in the x ray peak, an average of 253.6 per minute. The increase is due to interference from the 92.5 keV background gamma ray. Gamma spectroscopy software packages could possibly use the peak as a calibration point within 300 s, though this is much less clear than with the weak background. Operating procedures nearly always recommend at least 300 s background and calibration acquisitions.
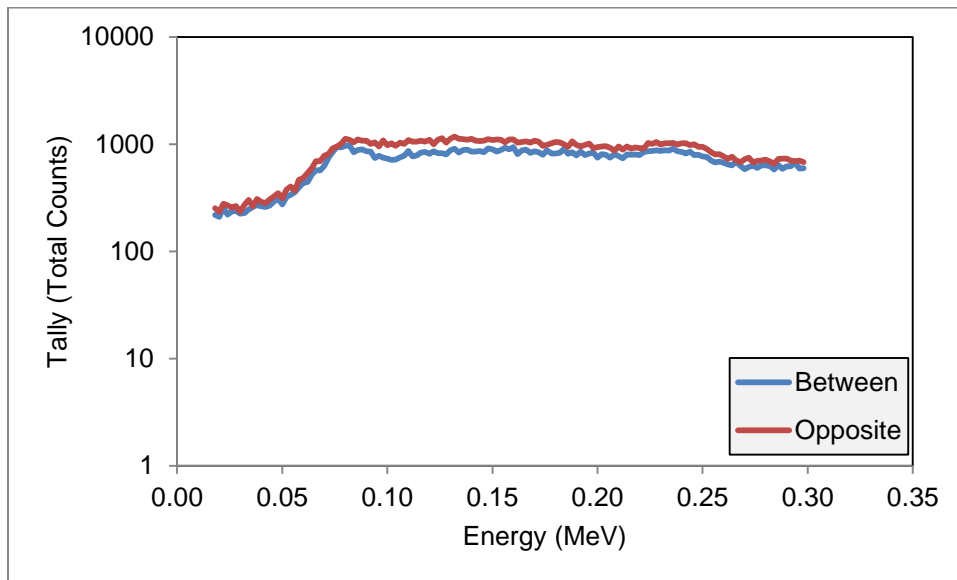
Fig. 5.12. Simulated 300 s spectral acquisition with 500 g potassium source and strong background source term.
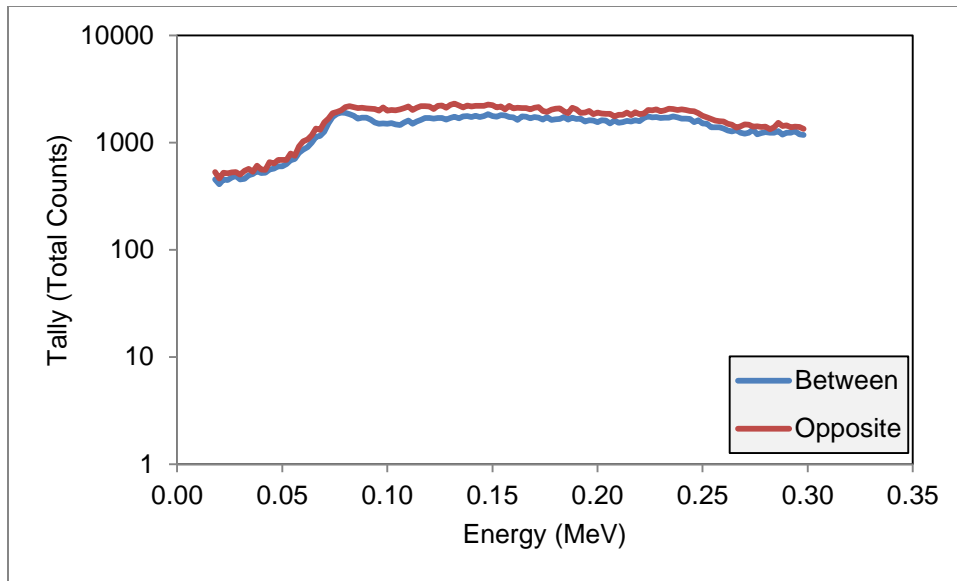
Fig. 5.13. Simulated 600 s spectral acquisition with 500 g potassium source and strong background source term.

5.4.   Americium-241 Interference

^{241}Am (432.2 year half-life) emits a 59.54 keV gamma ray with a 35.9% branching ratio. This gamma ray is not close enough to the 77.1 keV bismuth x ray for the peaks to overlap, but it can provide some problems for gamma spectroscopy algorithms. Keeping the peak width set at the 99% confidence level begins to overlap with the ^{241}Am peak. This overlap can sometimes cause negative CAC values because the linear method is being drawn onto the high-energy edge of the ^{241}Am peak. Reducing the peak width to the 95% or 90% confidence level removes this interference.

The x ray peak strength for the calibration source with a 1.85 kBq (0.05 μCi) point source of ^{241}Am located 50 cm from the center of the detector crystal is shown in Table 5.4. The calibration source has a significant shielding effect on ^{241}Am gamma ray

itself, as shown in Fig. 5.14, though it is not strong enough to shield higher-activity

[241]Am sources.

Table 5.4. X ray peak strength with 1.85 kBq (0.05 µCi) [241]Am point source located 50 cm from center of detector crystal.

[241]Am Source Location	K Mass (g)	CAC (s-1)	CAC σ	Time to reach 400 CAC (s)
Opposite	100	0.01	0.023	46176
	250	0.76	0.028	530
	500	1.58	0.039	253
	750	2.15	0.048	186
	1000	2.61	0.056	153
Same Side	100	0.17	0.014	2415
	250	0.81	0.023	496
	500	1.65	0.036	242
	750	2.32	0.046	172
	1000	2.83	0.054	141
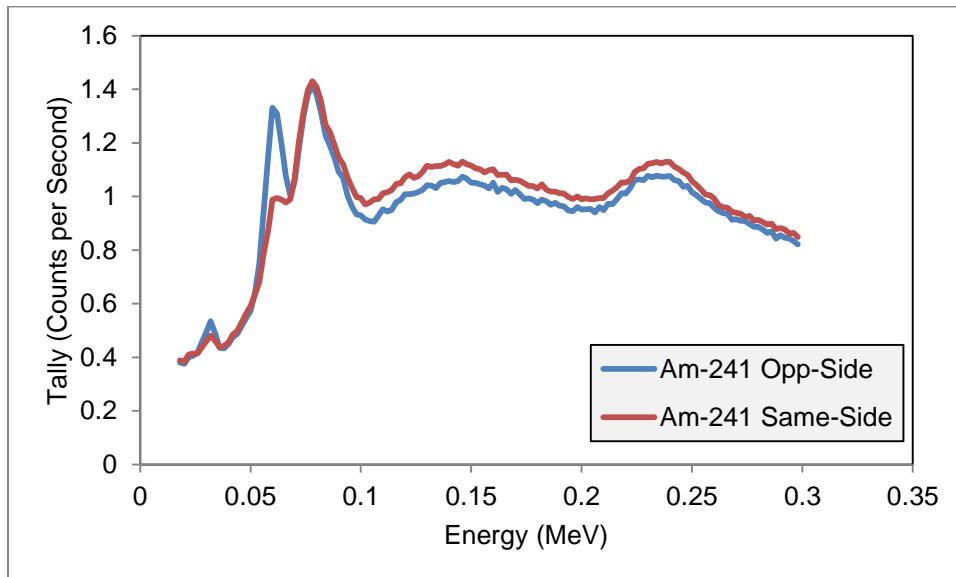
Fig. 5.14. Shielding effect of 500 g potassium calibration source on 1.85 kBq (0.05 µCi) [241]Am source.

5.5.   Alternative Source Configurations

Using the calibration source on only one side of the detector creates an asymmetric shielding effect on the detector response. In principle, splitting the source into two halves and placing the two halves on the 4 x 16 in^2 detector faces could slightly improve the x ray peak strength, as well as reduce the overall shielding effect by removing the asymmetry. Two split source configurations using bismuth powder as the x ray production agent were considered: one that used 50 wt% urethane as a binding agent, and one that used no binding agent and encased 92 wt% KCl and 8% bismuth powder in a 1-mm thick plastic sleeve. The first is referred to as the Split KCl-Bismuth Matrix (KBMS) source, and the second is referred to as the Plastic-encased Split KCl-Bismuth (PKBS) source.

5.5.1.   Split Source with Urethane Binding Agent

The KMBS source was simluated with a homogeneous mixture of 46 wt% KCl, 4 wt% bismuth metal powder, and 50 wt% urethane as a binding agent. The ratio of bismuth powder to natural potassium in the source was ~0.166. The 500 g potassium source is shown in Fig. 5.15.
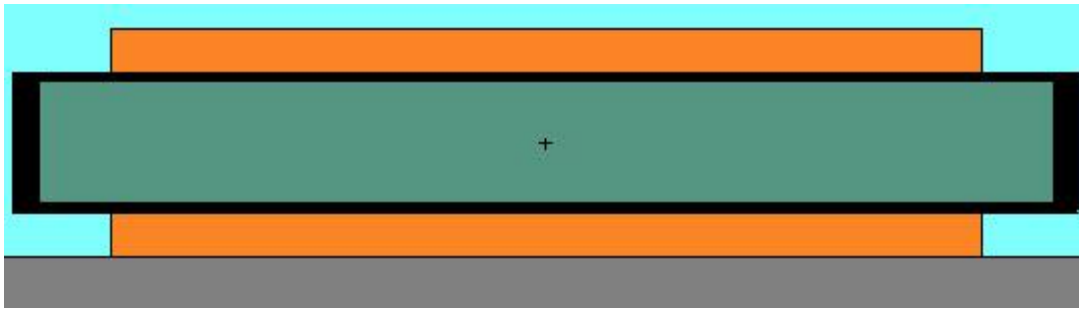
Fig. 5.15. Split source with urethane binding agent. The sources and detector are resting on top of a concrete slab.

The x ray peak strengths, shielding effects, and noise added to the NaI(Tl) spectrum are shown in Table 5.5 for several potassium masses of the KBMS source. The x ray peak is much stronger than the one-piece KBM source (3.62 ± 0.05 CAC s^{-1} versus 2.80 ± 0.04 CAC s^{-1} for 500 g potassium). This increase in source strength is due to reduced average distance from the x ray-producing bismuth atoms to the detector crystal. The overall shielding effect of the KBMS source is comparable to that of the KBM, but the KBMS shielding effect is split between the two detector faces.

Table 5.5. Performance measures for KBMS source in presence of weak background.

K Mass (g)	CAC (s^{-1})	CAC σ	Cal Source Total CPS	Cal Source Total CPS σ	% Bkg Change
100	0.58	0.025	142	0.027	-4.18%
250	1.70	0.033	324	0.063	-7.56%
500	3.62	0.050	572	0.115	-12.58%
750	5.22	0.065	768	0.154	-15.89%
1000	6.59	0.079	926	0.193	-18.26%

5.5.2. *Plastic-encased Split Source*

The calibration source was also simulated with no binding agent. A homogenous mixture of 92 wt% KCl salt and 8 wt% bismuth metal powder was placed in a 1-mm thick polypropylene (C_3H_6, 0.9 g cm^{-3}) sleeve (McConn et al. 2011). Polypropylene (PP) was selected because it is durable, temperature-resistant, easily moldable into virtually any desired shape, and can be made into a living hinge so the x ray producing contents can be added after the casing is molded. The ratio of bismuth to natural potassium was kept constant at ~0.166 (92 wt% KCl and 8 wt% bismuth). The density of this mixture was 2.6077 g cm^{-3}.

The plastic-encased 500 g potassium split source is shown in Fig. 5.16. The sleeve is shown as the gold outline with black border surrounding the source and detector. The casing was designed to stretch the entire length of the detector in order to make an easily reproducible geometry for calibration. The gaps on the ends of the source represent regions in the plastic which were hollowed out to reduce the weight.
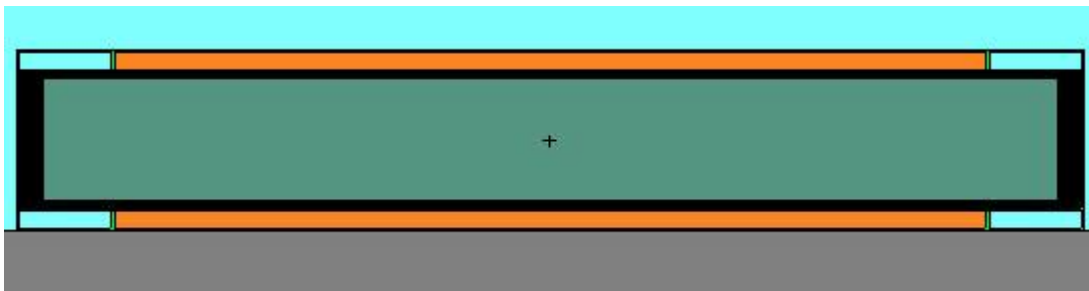
Fig. 5.16. Split source with plastic sleeve.

The advantages of this arrangement are that the source can be made thinner and lighter due to the removal of extraneous binding material while using more potassium and bismuth, and that the PKBS source can be removed from the detector for sensitive measurements. The disadvantage of removing the PKBS source is that the gain could drift over the course of longer measurements, so the source must be used for recalibration periodically.

The simulated PKBS performance measures are shown in Table 5.6. The plastic-encased split source induces a greater CAC response in the detector than does any configuration with a binding agent. This is because the potassium and bismuth are, on average, closer together, and thus undergo more x ray production interactions. The shielding effect is slightly reduced compared to both the KBM and KBMS sources due to the thinner source construction. This is balanced by an approximately 10% increase in the total noise added to the detector spectrum by the PKBS source.

Table 5.6. Performance measures for PKBS source in presence of weak background.

K Mass (g)	CAC (s-1)	CAC σ	Cal Source Total CPS	Cal Source Total CPS σ	% Bkg Change
100	0.98	0.025	131	0.031	-4.58%
250	2.79	0.036	319	0.074	-7.49%
500	6.13	0.058	602	0.142	-11.28%
750	9.02	0.079	857	0.204	-14.39%
1000	11.34	0.098	1087	0.248	-16.84%
1250	13.15	0.114	1296	0.301	-18.91%
1500	14.67	0.130	1488	0.350	-20.57%

The simulated CAC response is shown in Fig. 5.17 for the three bismuth-based source configurations. The PKBS source shows the most CAC in the x ray peak by a considerable margin over the other two source configurations.
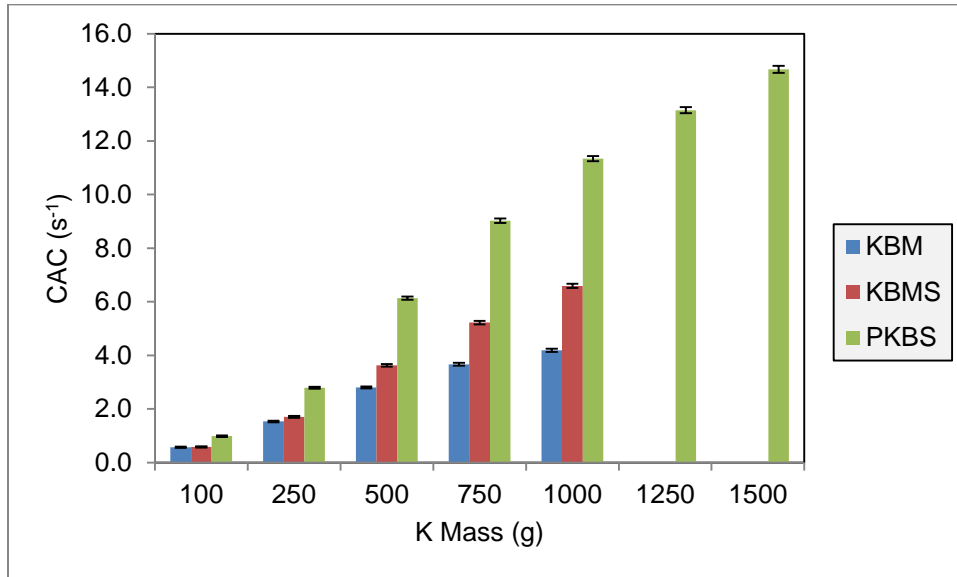
Fig. 5.17. Comparison of CAC response for three simulated bismuth-based source configurations.

The noise added to the overall detector spectrum is shown in Fig. 5.18. for the three bismuth-based source configurations. The split source configurations add considerably more noise to the spectrum than the single KBM source, but this increase in detector noise is balanced by the increase in the CAC, especially for the PKBS source.
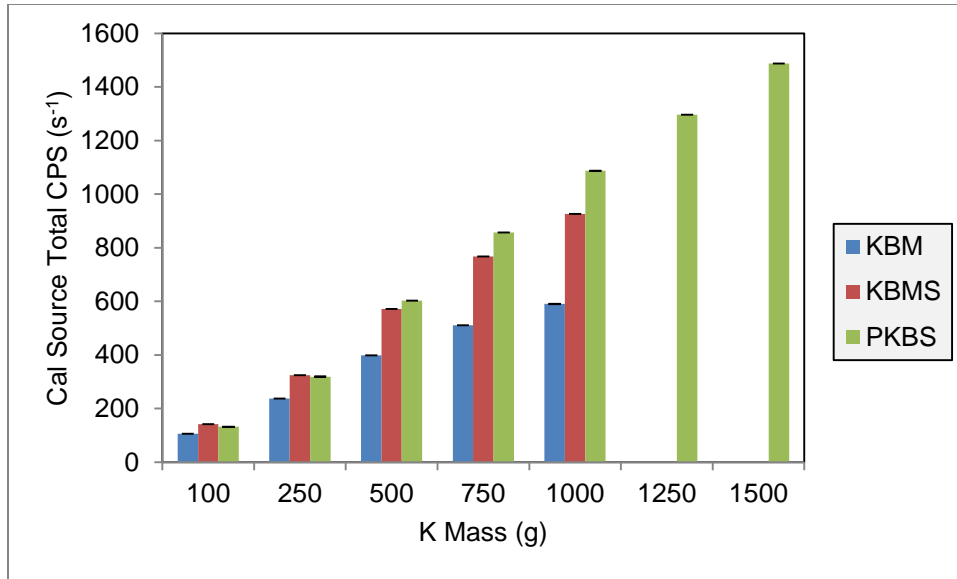
Fig. 5.18. Total noise added to NaI(Tl) spectrum for three simulated bismuth-based source configurations.

Fig. 5.19 shows that the split sources drastically reduce the shielding effect by the calibration source on the simulated weak background source term. Please note, however, that this background source term was only modeled from one direction. Because of the split source symmetry, the overall shielding effect is comparable for the all three bismuth-based sources.
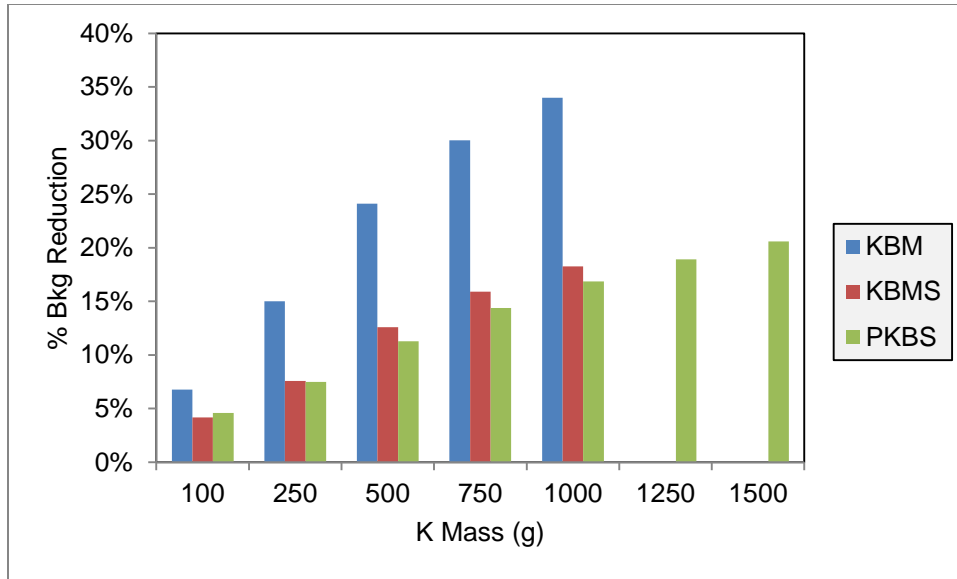
Fig. 5.19. Shielding effect of three simulated bismuth-based source configurations on weak background source term.

5.6. Dose Calculations

The whole-body dose rates for the KBM, KMBS, and PKBS sources were calculated in air at 0.1 cm (effectively a contact measurement) and 30.48 cm. The air dose rates are made up of the sum of the photon dose, electron dose, and the dose from photons created from electron source particles. All dose rates are reported in terms of dose to tissue.

The total contact dose rates are shown in Fig. 5.20 with 1σ error bars. The three source configurations show no statistically significant difference in their simulated dose rates within 2σ. The only exception is that the 100 g potassium case for the KBMS and PKBS sources shows no statistically significant difference within 3σ. These dose rates, and their uncertainties, are dominated by electron dose, as shown in Fig. 5.21. This

dominance of the electron component in the overall dose rate held for all three bismuth-based source configurations.

The maximum simulated contact dose rate was 1.08 ± 0.147 μSv hr^{-1} (108 ± 14.7 μrem hr^{-1}). Assuming continuous exposure at these levels, the maximum dose rate delivered over one year would be 9.5 mSv (0.95 rem), which is only one-half that of the International Commission on Radiological Protection (ICRP) Publication 103 recommendations for occupational exposure. The calibration source thus would deliver an extremely small dose to the extremities of workers handling the source.
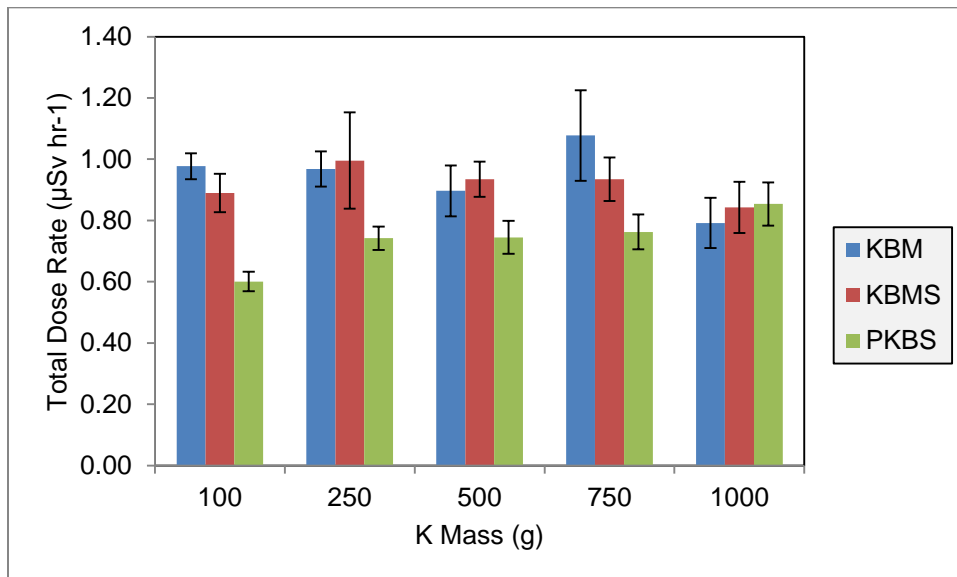
Fig. 5.20. Comparison of total dose rate at 0.1 cm (contact measurement). All error bars are $\pm 1\sigma$.
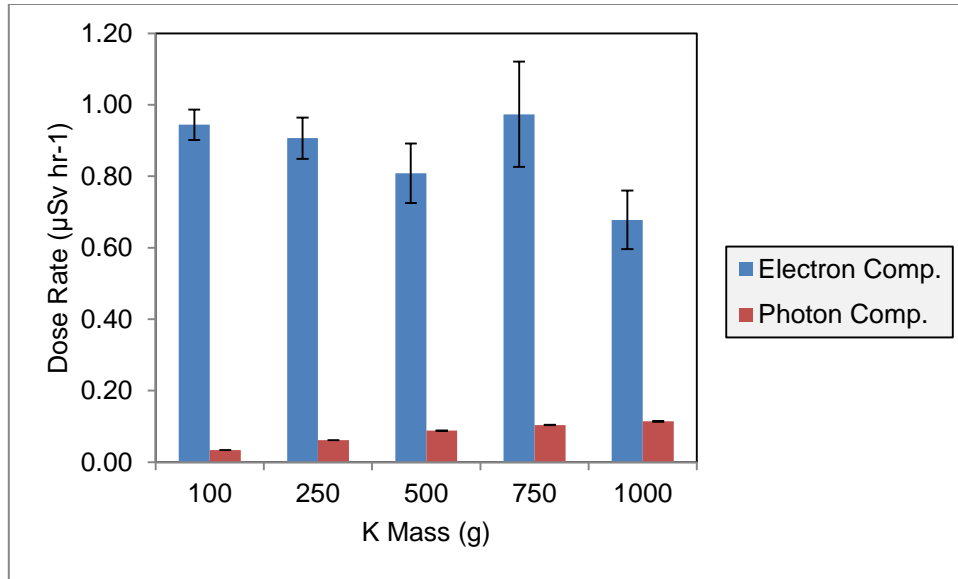
Fig. 5.21. Electron and photon components of dose rate at 0.1 cm (contact) for KBM source.

The simulated total dose rates at 30.48 cm are shown in Fig. 5.22. The dose rates for the three bismuth-based sources agree in all cases within 2σ. The dose rate is again dominated by the electron dose. The maximum dose rate calculated at 30.48 cm was 0.0547 ± 0.0015 µSv hr^{-1} (5.47 ± 0.15 µrem hr^{-1}), roughly equivalent to the background dose rate in most terrestrial areas.
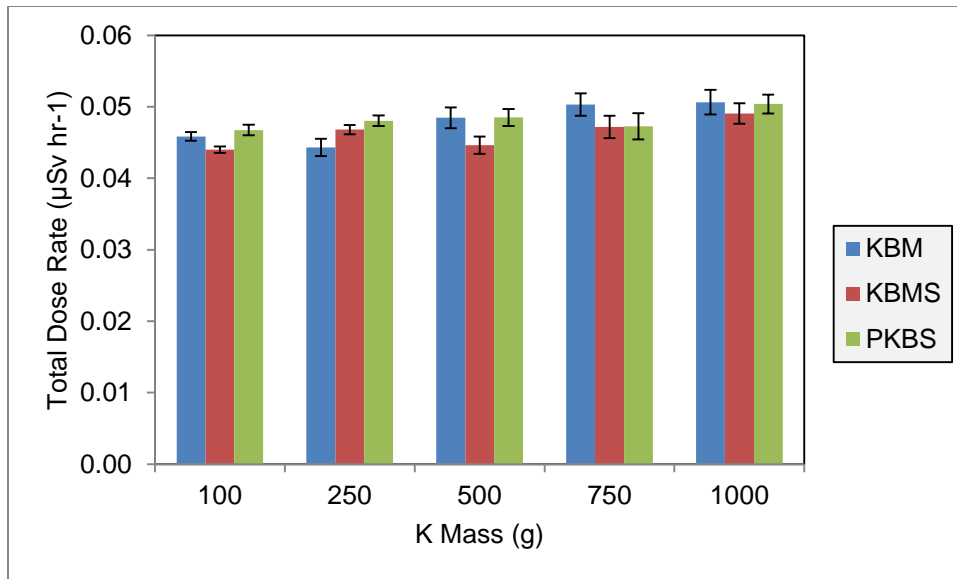
Fig. 5.22. Comparison of total dose rate at 30.48 cm (1 foot).

These calibration source dose rates at contact and 30.48 cm can be compared to the dose rates of exempt-quantity ^{60}Co and ^{137}Cs check sources. The check sources were modeled as point sources embedded in the center of polypropylene disks 2.54 cm in diameter and 0.5 cm thick. The photon doses were measured using the same F5 tallies as the calibration source gamma doses. The exempt quantity activities for each are found in Table 1.1.

The calculated check source dose rates are shown in Table 5.7. The exempt quantity dose rates at contact are four orders of magnitude larger than the calibration source dose rate, and the dose rates at 30.48 cm are two orders of magnitude larger. The activity of the 1000 g potassium source (31 kBq) is comparable to that of the ^{60}Co exempt quantity source (37 kBq); the difference in dose rates is due to the substantial

fraction of beta particles that are absorbed in the calibration source itself, and the fact

that ^{60}Co emits two gamma rays for every decay event.

Table 5.7. Calculated exempt quantity photon source dose rates at contact and 30.48 cm, for comparison with calibration source dose rates.

Isotope	Activity (kBq)	Distance (cm)	Gamma Dose Rate (μSv hr^{-1})	Gamma Dose Rate σ (μSv hr^{-1})	Gamma Dose Rate (μrem hr^{-1})
^{60}Co	37	0.1	9.39×10^{2}	9.39×10^{-2}	9.39×10^{4}
		30.48	1.22×10^{-1}	1.22×10^{-5}	1.22×10^{1}
^{137}Cs	370	0.1	2.38×10^{3}	2.38×10^{-1}	2.38×10^{5}
		30.48	3.12×10^{-1}	6.24×10^{-5}	3.12×10^{1}

Routine handling of the calibration source thus would represent an extremely small contribution to the worker's overall dose, likely less than equivalent handling of an exempt quantity check source. This increase in the worker's accumulated dose would almost certainly be hidden within variances in the natural background exposure.

77

6. CONCLUSIONS

A gamma calibration source is proposed that uses KCl salt and a high-Z metal to create a two-point calibration for a NaI(Tl) field gamma spectroscopy instrument. The Department of Energy has ruled that all sealed radioactive sources, even those considered exempt under NRC regulations, are subject to radioactive material controls. These controls include transportation and shipping restrictions, end-of-life treatment, and disposal as hazardous waste. However, sources based on the ubiquitous, primordial isotope ^{40}K (half-life 1.248×10^9 years) are not subject to these restrictions. This work details the design of a ^{40}K-based field calibration source, in collaboration with Sandia National Laboratory.

The ^{40}K-based field calibration source was designed according to the following criteria. As the source is not intended to be removed from the detector during measurements, the source should maximize the production of x rays while minimizing any addition to the Compton and bremsstrahlung continua, and thus to the total count rate. The source should be easily portable with any 2 x 4 x 16 inch^3 NaI(Tl) instrument, adding as little weight and bulk to the detector system as possible. The calibration source could be redesigned for other NaI(Tl) or high-purity germanium field spectrometers.

The MCNPX transport code was used to statistically model a coupled electron-photon system that included a NaI(Tl) detector and a calibration source. The x ray production of two methods was explored: in a high-Z layer (HZL) interposed between the source and detector, and in a KCl-bismuth matrix (KBM). In each, several

78

parameters were varied in order to maximize the production of x rays while minimizing the total count rate and shielding effect.

The areal dimensions of the source were fixed such that 75% of the NaI(Tl) crystal's largest face was covered. The thickness was varied by using units of electron range for the high-Z layer configuration and the mean free path of the 77.1 keV bismuth x ray for the bismuth powder configuration, in order to make the source dependent on matrix density and thickness rather than on composition.

In both calibration source configurations, the gamma component of the x ray peak increased virtually linearly with increasing source matrix thickness, while the beta component gradually reached a point of saturation. Adding more potassium source material thus reaches a point of diminishing returns, where adding more source material contributes less to the x ray peak strength.

The optimal high-Z layer thickness was determined to be ~0.25 mean free paths of the corresponding $K_{\alpha 1}$ x ray, regardless of the metal used. The relative x ray peak strength showed a direct correlation with increasing Z.

The x ray peak response for the KBM reached a plateau when the bismuth-potassium mass ratio was between 0.1 and 0.2. For constant source dimensions and proportions of bismuth and potassium, the x ray peak response varied inversely with the amount of binding agent present.

The two configurations were compared based on tally count rates in the respective x ray peak bins, and through comparison of their pulse-height spectral characteristics. Concrete background source terms from the work of Ryan (2011) were

used to simulate an open, single-source background environment like that of an open concrete pad with no cosmic background. Using equal amounts of potassium, the KBM configuration produced more counts in the peak bin than any high-Z layer configuration. Lead and gold were the two best-performing HZL metals, but lead is a toxicity hazard and gold is substantially more expensive than the other metals considered. The KBM configuration was chosen as the development model because it is cheap, nontoxic, and performs well in simulation.

The counts above continuum (CAC) and the calibration source's shielding effect were measured using the linear method for several potassium masses in the KBM configuration in the presence of two concrete background source terms. As more potassium is added, the source becomes thicker and a more effective shield, which creates an asymmetrical response to external sources. The shielding effect can be useful for separating the x ray peak from background, but it can reduce the detector's sensitivity to external sources. Using more potassium also creates more total counts across the pulse-height spectrum, which also reduces sensitivity to low-activity and low-energy sources. The KBM source with 500 g potassium was chosen as the basis for further development based on its relatively high CAC.

The detector's response to [241]Am gamma rays in the presence of the calibration source was simulated by placing a 59.54 keV point source 50 cm from the center of the detector crystal, above the top face of the detector. Using the 99% peak bin width setting for the x ray peak caused an interference with the [241]Am peak, leading to incorrect CAC results. Using a bin width that uses the 95% and 90% confidence intervals for the 77.1

keV bismuth x ray peak resolved this interference. A simulated 1.85 kBq (0.05 μCi) ^{241}Am source significantly degraded the x ray peak strength, and larger sources can nearly drown out the x ray signal entirely.

Simulations were performed in order to model the statistical appearance of the pulse-height spectra for the 500 g potassium source during 60 s, 300 s, and 600 s spectral acquisitions. Both the weak and strong background sources were included. The simulations concluded that gamma spectroscopy software would be able to perform a two-point calibration before 300 s in weak background environments. Acquisitions in stronger background environments could require up to 600 s to obtain a calibration peak. In either case, the x ray peak strength was not enough for the source to function as a gain stabilization source.

Two split sources were simulated in order to resolve the asymmetric shielding effect and improve the x ray peak CAC. The first split source (KBMS) used the same binding material composition as the united source. The second split source (PKBS) removed the binding material and placed the same relative proportions of bismuth and KCl into a 1-mm thick polypropylene sleeve. The PKBS source had a significantly stronger x ray CAC than either the baseline KBM source or the split KBMS source. The overall noise in the detector spectrum was increased by splitting the source, but this was offset by the increase in CAC, especially in the PKBS source. Splitting the source equalized the shielding effect across the two largest faces of the detector.

The maximum dose rate for the calibration source at 30.48 cm (1 foot) was calculated to be 0.0547 ± 0.0015 μSv hr^{-1} (5.47 ± 0.15 μrem hr^{-1}), which is roughly

equivalent the natural background exposure in most terrestrial areas. This dose rate is roughly two orders of magnitude less than that of a ^{137}Cs exempt quantity check source measured at the same distance. Within 2σ, there is no statistically significant difference in the simulated dose rate between the KBM, KMBS, and PKBS sources at 30.48 cm. The dose delivered is mainly from the source electrons. The dose to workers handling the calibration source would be extremely small, and would likely be hidden in the variations of the background exposure.

This research may be improved by several means. First, no experimental validation of the MCNPX results was performed. The performance of a physical calibration source/detector system is not expected to differ from these simulation results by more than 10%, but experimental validation should be performed anyway. Losses of signal in detector electronics, though small in most modern systems, were not modeled.

Second, background source terms are highly variable based on location, altitude, and the presence of nearby structures. The background source terms in this study only emitted photons from one side of the source/detector system. They were modeled on concrete from Oak Ridge National Laboratory characterized by Ryan (2011), and may not be representative of background at Sandia National Laboratory or Texas A&M University.

Third, only one dimension of the system's directional response to external sources was studied. The response relative to a detector with the calibration source removed is expected to be at a maximum on the 2 x 16 in^2 and 2 x 4 in^2 faces and at a minimum at 45° to the calibration source's normal plane.

In conclusion, the most effective calibration source within the parameter space explored uses a homogeneous mixture of 1902 g of KCl salt (1000 g potassium) and 165.8 g of bismuth powder split between two 1-mm thick polypropylene sleeves. This calibration source produces a strong x ray peak while producing relatively few extraneous total counts to the rest of the spectrum. It is not subject to DOE restrictions, and would serve as a light, cheap, field calibration source that could function in all but the highest-background areas.

REFERENCES

ANSI/ANS-6.1.1-1991;W2001: Neutron and gamma-ray fluence-to-dose factors.

Attix FH. Introduction to radiological physics and radiation dosimetry. Weinheim:
Wiley VCH; 2004.

Begemann F, Ludwig KR, Lugmair GW, Min K, Nyquist LE, Patchett PJ, Renne PR,
Shih CY, Villa IM, Walker RJ. Call for an improved set of decay constants for
geochronological use. Geochemica et Cosmochimica Acta 85.1:111-121; 2001.

Berger MJ, Hubbell JH, Seltzer SM, Chang J, Coursey JS, Sukumar R, Zucker DS,
Olsen K, National Institute of Standards and Technology. XCOM: photon cross
sections database. NIST Standard Reference Database 8 [online]. 1998, updated
Nov 2010. Available at nist.gov/pml/data/xcom/index.html. Accessed 9 April
2012.

Burnett DS, Lippolt HJ, Wasserburg GJ. The relative isotopic abundance of K^{40} in
terrestrial and meteoric samples. Journal of Geophysical Research 71.4:1249-
1269; 1966.

Eckerman KF, Westfall RJ, Ryman JC, Cristy M. Availability of nuclear decay data in
electronic form, including beta spectra not previously published. Health Phys
67(4):338-345; 1994.

Evans RD. The atomic nucleus. New Delhi: McGraw-Hill; 1955.

Firestone RB, Ekstrom LP, LBNL Isotopes Project – LUNDS Universitet. WWW table of radioactive isotopes [online]. 2004. Available at ie.lbl.gov/toi. Accessed 6 Mar 2012.

Hakimabad HM, Panjeh H, Vejdani-Noghreiyan A. Nonlinear response function of a 3x3 in. nai scintillation detector. Asian J Exp Sci 21.1:1-12; 2007.

Health Physics Society (HPS) Science Support Committee. Guidance for the use of exempt quantities of radioactive materials in secondary school [online]. Aug 2010. Available at hps.org/sciencesupport. Accessed 6 Apr 2012.

Hubbell JH, Seltzer SM, National Institute of Standards and Technology. Tables of x-ray mass attenuation coefficients and mass energy-coefficients from 1 keV to 20 MeV for elements Z=1 to 92 and 48 additional substances of dosimetric interest [online]. 2004. Available at nist.gov/pml/data/xraycoeff/. Accessed 6 Mar 2012.

International Commission on Radiological Protection (ICRP). The 2007 recommendations of the International Commission on Radiological Protection. New York: Elsevier; ICRP Publication 103; Ann. ICRP 37(2– 4); 2007.

Jung JW. ^{142}Pr glass seeds for the brachytherapy of prostate cancer. Diss. Texas A&M University. May 2007.

Kallenbach GA. 2012 Private Communication (Sandia National Laboratory).

Kaste JM, Bostick BC, Heimsath AM. Determining ^{234}Th and ^{238}U in rocks, soils, and sediments via the doublet gamma at 92.5 keV. The Analyst 131: 757-761; 2006.

Katz L, Penfold AS. Range-energy relationships for electrons and the determination of beta-ray end-point energies by absorption. Reviews of Modern Physics 24.1: 28-44; 1952.

Knoll GF. Radiation detection and measurement, 3rd ed. New York: Wiley & Sons; 2000.

McConn RE, Gesh CJ, Pagh RT, Rucker RA, Williams RG. Compendium of material composition data for radiation transport modeling. PNNL-15870 Rev. 1. 4 Mar 2011.

National Nuclear Data Center (NNDC), Brookhaven National Laboratory (BNL). Chart of nuclides [online]. 2004. Available at nndc.bnl.gov/nudat2. Accessed 5 Mar 2012.

Pelowitz DB, ed. MCNPX user's manual, version 2.6.0. Los Alamos National Laboratory; 2008.

Radiation Dose Assessment Resource (RADAR). On-line decay data [online]. 2003. Available at doseinfo-radar.com/RADARDecay.html. Accessed 9 Mar 2012.

Ryan CM. Determining the impact of concrete roadways on gamma ray background readings for radiation portal monitor systems. MS thesis. Texas A&M University. May 2011.

Shultis JK, Faw RE. An MCNP primer [online]. 12 Dec 2011. Available at web.utk.edu/~rpevey/public/NE406/. Accessed 1 Sep 2012.

Turner JE. Atoms, radiation, and radiation protection, 3rd ed. Weinheim: Wiley VCH; 2007.

U.S. Department of Energy (DOE). Radiation protection programs guide. Washington, DC: U.S. Government Printing Office; DOE G 441.1-1B; 2007.

U.S. Geological Survey (USGS). Commodity statistics and information [online]. 27 May 2011. Available at minerals.usgs.gov/minerals/pubs/commodity/. Accessed 16 Sep 2012.

U.S. Nuclear Regulatory Commission (NRC). Rules of general applicability to domestic licensing of byproduct material. Washington, DC: U.S. Government Printing Office; 10 CFR Part 30.18; 2008.

APPENDIX

A.1. Example MCNPX Input Deck for HZL, Beta Component

```
HZL Cal Source with 0.25mfp Gold Target, Beta Component
c                                                                   #
c   Built by:   Jeremy Rogers                                       #
c               Texas A&M University                                #
c               jl.rogers@tamu.edu                                  #
c                                                                   #
c High-Z layer geometry, 0.25 mfp Au (0.0037 cm)                    #
c 50 wt% KCl, 50 wt% urethane matrix                                #
c KCl matrix is 3.737 cm thick (10 electron ranges)                 #
c
c Cell Cards
10  1 -3.667    10 -11  12 -13  14 -15    imp:e=1 imp:p=2 $ NaI crystal
11  5 -2.25     26 -27  28 -29  30 -31
                (-10:11:-12:13:-14:15)    imp:e=1 imp:p=2 $ Teflon filling
20  2 -8.00     20 -21  22 -23  24 -25
                (-26:27:-28:29:-30:31)    imp:e=1 imp:p=2 $ 304L stainless
40  4 -1.5420   40 -41  42 -43  50 -44    imp:e=1 imp:p=1 $ KCl cal source
50  3 -19.29    40 -41  42 -43  25 -50    imp:e=1 imp:p=1 $ Au metal
99  6 -1.205e-3 #10 #11 #20 #40 #50 -99   imp:e,p=1 $ Surrounding void
100 0                               99    imp:e,p=0 $ Point of Know Return
c Blank card follows >>>

c Surface Cards
c NaI crystal
10 px -20.32
11 px  20.32
12 py -5.08
13 py  5.08
14 pz -2.54
15 pz  2.54
c S/S housing, PMT excluded
20 px -21.43125
21 px  21.43125
22 py -5.3975
23 py  5.3975
24 pz -2.8575
25 pz  2.8575
26 px -21.32965
27 px  21.32965
28 py -5.2959
29 py  5.2959
30 pz -2.7559
31 pz  2.7559
c KCl Seed Source
40 px -17.4985
41 px  17.4985
42 py  -4.4070
43 py   4.4070
44 pz   6.5986
c Interpolating Metal
50 pz   2.86121
```

88

```
c Point of Know Return
99 so   100
c Blank card follows >>>

c Data Cards
mode p e
c Source definition
sdef x=d1 y=d2 z=d3 erg=1.460822 par=2
si1 -17.4985 17.4985      $ X-dimension sampling limits
sp1 0 1                   $ Uniform probability distribution
si2 -4.4070 4.4070        $ Y-dimension sampling limits
sp2 0 1                   $
si3 2.86121 6.5986        $ Z-dimension sampling limits
sp3 0 1                   $
si4 A 0 3.28E-02 9.84E-02 1.64E-01 2.30E-01 2.95E-01  $ Source energy tab.
      3.61E-01 4.26E-01 4.92E-01 5.57E-01 6.23E-01
      6.89E-01 7.54E-01 8.20E-01 8.85E-01 9.51E-01
      1.02E+00 1.08E+00 1.15E+00 1.21E+00 1.28E+00
sp4   0 2.96E-02 3.70E-02 4.34E-02 4.89E-02 5.35E-02  $ Source prob. dist.
      5.71E-02 5.99E-02 6.17E-02 6.26E-02 6.25E-02
      6.14E-02 5.92E-02 5.61E-02 5.18E-02 4.62E-02
      3.92E-02 3.05E-02 2.03E-02 1.00E-02 1.83E-03
c
c CUT cards
cut:e j 0.02
cut:p j 0.02
c
c Material Cards (from PNNL 15870 Rev1, except where noted)
c
c Sodium iodide (3.667 g/cc)
m1   11000  0.5
     53000  0.5
c Steel, Stainless 304L (8.00 g/cc)
m2    6000 -0.00015   $ C
     14000 -0.00500   $ Si
     15031 -0.00023   $ P
     16000 -0.00015   $ S
     24000 -0.19000   $ Cr
     25000 -0.01000   $ Mn
     26000 -0.69448   $ Fe
     28000 -0.10000   $ Ni
c Gold (19.3 g/cc)
m3   79000 1.0        $ Au (19.3 g/cc)
c Mixture of 50 wt% KCl and 50 wt% urethane (1.5420 g/cc)
m4    1000 -0.03960   $ H
      6000 -0.20222   $ C
      7000 -0.07861   $ N
      8000 -0.17958   $ O
     17000 -0.23778   $ Cl
     19000 -0.26222   $ K
c Polytetrafluoroethylene (PTFE, Teflon) (2.25 g/cc)
m5    6000 0.333339   $ C
      9019 0.666661   $ F
c Air, dry, near sea level (1.205e-3 g/cc)
m6    6000  -0.000124 $ C
      7014  -0.755268 $ N
      8016  -0.231781 $ O
      18000 -0.012827 $ Ar
c
```

```
c Detector Tallies
c
c Overall Pulse Height Spectrum w/ Gaussian Energy Broadening for Generic NaI
F8:P 10
E8 0 1E-04 0.002 348i 0.7 20.0
FT8 GEB -0.00789 0.06769 0.21159
c
c X-ray Peak PH Spectrum w/ GEB (Beta, Bi)
F18:P 10
E18 0 1E-04 0.058017 0.079575 20.0
FT18 GEB -0.00789 0.06769 0.21159
c
c MCNPX will run for 1e8 particle histories
nps 1e8
c Blank card follows >>>
```

A.2. Example MCNPX Input Deck for KBM, Gamma Component

```
KBM Cal Source with 5wt% Bi Content, Gamma component
c                                                                       #
c   Built by:    Jeremy Rogers                                          #
c               Texas A&M University                                    #
c               jl.rogers@tamu.edu                                      #
c                                                                       #
c KCl/Bi matrix geometry, 5 wt% Bi                                      #
c 45 wt% KCl, 50 wt% urethane matrix                                    #
c KCl matrix is 2.171 cm thick (10 mfp of 77.1 keV Bi x-ray)           #
c
c Cell Cards
10  1 -3.667     10 -11  12 -13  14 -15      imp:e,p=1 $ NaI crystal
11  5 -2.25      26 -27  28 -29  30 -31
                 (-10:11:-12:13:-14:15)      imp:e,p=1 $ Teflon filling
20  2 -8.00      20 -21  22 -23  24 -25
                 (-26:27:-28:29:-30:31)      imp:e,p=1 $ 304L stainless steel
40  4 -1.9318    40 -41  42 -43  25 -44      imp:e,p=1 $ KCl cal source
99  6 -1.205e-3  #10 #11 #20 #40    -99      imp:e,p=1 $ Surrounding void
100 0                                99      imp:e,p=0 $ Point of Know Return
c Blank card follows >>>

c Surface Cards
c NaI crystal
10 px -20.32
11 px  20.32
12 py -5.08
13 py  5.08
14 pz -2.54
15 pz  2.54
c S/S housing, PMT excluded
20 px -21.43125
21 px  21.43125
22 py -5.3975
23 py  5.3975
24 pz -2.8575
25 pz  2.8575
26 px -21.32965
27 px  21.32965
28 py -5.2959
29 py  5.2959
30 pz -2.7559
31 pz  2.7559
c KCl Seed Source
40 px -17.4985
41 px  17.4985
42 py  -4.4070
43 py   4.4070
44 pz   3.0351
45 pz   3.2128
46 pz   3.3904
47 pz   3.5680
48 pz   3.7457
49 pz   3.9233
50 pz   4.1009
51 pz   4.2786
52 pz   4.4562
53 pz   4.6338
```

```
c Point of Know Return
99 so    100
c Blank card follows >>>

c Data Cards
mode p e
sdef x=d1 y=d2 z=d3 erg=d4 par=3
si1 -17.4985 17.4985
sp1 0 1
si2 -4.4070 4.4070
sp2 0 1
si3 2.8575 4.6338
sp3 0 1
si4 A 0 3.28E-02 9.84E-02 1.64E-01 2.30E-01 2.95E-01
       3.61E-01 4.26E-01 4.92E-01 5.57E-01 6.23E-01
       6.89E-01 7.54E-01 8.20E-01 8.85E-01 9.51E-01
       1.02E+00 1.08E+00 1.15E+00 1.21E+00 1.28E+00
sp4    0 2.96E-02 3.70E-02 4.34E-02 4.89E-02 5.35E-02
       5.71E-02 5.99E-02 6.17E-02 6.26E-02 6.25E-02
       6.14E-02 5.92E-02 5.61E-02 5.18E-02 4.62E-02
       3.92E-02 3.05E-02 2.03E-02 1.00E-02 1.83E-03
c
c CUT cards
cut:e j 0.02
cut:p j 0.02
c Material Cards (from PNNL 15870 Rev1, except where noted)
c
c Sodium iodide (3.667 g/cc)
m1   11000  0.5
     53000  0.5
c
c Steel, Stainless 304L (8.00 g/cc)
m2    6000 -0.00015   $ C
     14000 -0.00500   $ Si
     15031 -0.00023   $ P
     16000 -0.00015   $ S
     24000 -0.19000   $ Cr
     25000 -0.01000   $ Mn
     26000 -0.69448   $ Fe
     28000 -0.10000   $ Ni
c
c Gold (19.3 g/cc)
m3   79000 1.0        $ Au (19.3 g/cc)
c
c Mixture of 50 wt% urethane, 45 wt% KCl, 5 wt% Bi (1.9318 g/cc)
m4    1000 -0.03960   $ H
      6000 -0.20222   $ C
      7000 -0.07861   $ N
      8000 -0.17958   $ O
     17000 -0.21400   $ Cl
     19000 -0.23600   $ K
     83000 -0.05      $ Bi
c
c Polytetrafluoroethylene (PTFE, Teflon) (2.25 g/cc)
m5    6000 0.333339   $ C
      9019 0.666661   $ F
c
c Air, dry, near sea level (1.205e-3 g/cc)
m6    6000  -0.000124 $ C
```

```
      7014  -0.755268 $ N
      8016  -0.231781 $ O
      18000 -0.012827 $ Ar
c
c Concrete (from Ryan) (density 2.301 g/cc)
m7   06000  -0.000500 $ C
     08000  -0.473100 $ O
     11000  -0.020000 $ Na
     12000  -0.003594 $ Mg
     13000  -0.066000 $ Al
     14000  -0.295200 $ S
     19000  -0.032700 $ P
     20000  -0.089800 $ Ca
     25000  -0.001153 $ Mn
     26000  -0.019100 $ Fe
c
c Polypropylene, C3H6 (0.9 g/cc)
m8    1001  -0.143711 $ H
      6000  -0.856289 $ C
c
c Water, Liquid (1.0 g/cc)
m9    1001  0.666657 $ H
      8016  0.333343 $ O
c
c Detector Tallies
c
c Overall Pulse Height Spectrum w/ Gaussian Energy Broadening for Generic NaI
F8:P 10
E8 0 1E-04 0.002 848i 1.7
FT8 GEB -0.00789 0.06769 0.21159
c
c X-ray Peak PH Spectrum w/ GEB (Gamma, Bi)
F18:P 10
E18 0 1E-04 0.065169 0.089045 1.368290 1.553354 20.0
FT18 GEB -0.00789 0.06769 0.21159
c
c MCNP will run for 1e8 particles
nps 1e8
c Blank card follows >>>
```

A.3.   Example MCNPX Input Deck for KBPS, Gamma Component

```
KBPS Test with 500 g K, 4 wt% Bi (Gamma Component)
c                                                                     #
c   Built by:   Jeremy Rogers                                         #
c               Texas A&M University                                  #
c               jl.rogers@tamu.edu                                    #
c                                                                     #
c Plastic-encased KCl/Bi matrix geometry                              #
c 92 wt% KCl, 8 wt% Bi matrix (2.6077 g/cc)                           #
c
c Cell Cards
10  1 -3.667    10 -11  12 -13  14 -15     imp:e,p=1 $ NaI crystal
11  5 -2.25     26 -27  28 -29  30 -31  & $
                (-10:11:-12:13:-14:15)     imp:e,p=1 $ Teflon filling
20  2 -8.00     20 -21  22 -23  24 -25  & $
                (-26:27:-28:29:-30:31)     imp:e,p=1 $ 304L stainless steel
40  4 -2.6077   40 -41  42 -43  50 -24     imp:e,p=1 $ KCl cal source, bottom
41  4 -2.6077   40 -41  42 -43  25 -51     imp:e,p=1 $ KCl cal source, top
60  8 -0.9000   20 -21  22 -23  66 -67  & $
                (-10:11:-12:13:-14:15)  & $
                (-26:27:-28:29:-30:31)  & $
                (-20:21:-22:23:-24:25)  & $
                (-40:41:-42:43:-50:24)  & $
                (-40:41:-42:43:-25:51)  & $
                (-26:60:-28:29:-50:24)  & $
                (-61:27:-28:29:-50:24)  & $
                (-26:60:-28:29:-25:51)  & $
                (-61:27:-28:29:-25:51)     imp:e,p=1 $ Plastic sleeve
61  6 -1.205e-3  26 -60  28 -29  50 -24    imp:e,p=1 $ Air gap 1
62  6 -1.205e-3  61 -27  28 -29  50 -24    imp:e,p=1 $ Air gap 2
63  6 -1.205e-3  26 -60  28 -29  25 -51    imp:e,p=1 $ Air gap 3
64  6 -1.205e-3  61 -27  28 -29  25 -51    imp:e,p=1 $ Air gap 4
90  7 -2.301    -90 -66  91                imp:e,p=1 $ Concrete
99  6 -1.205e-3 #10 #11 #20 #40 #41 #60  & $
                   #61 #62 #63 #64 #90 -99  imp:e,p=1 $ Surrounding void
100 0                               99 imp:e,p=0 $ Point of Know Return
c Blank card follows >>>

c Surface Cards
c NaI crystal
10 px -20.32
11 px  20.32
12 py -5.08
13 py  5.08
14 pz -2.54
15 pz  2.54
c S/S housing, PMT excluded
20 px -21.43125
21 px  21.43125
22 py -5.3975
23 py  5.3975
24 pz -2.8575
25 pz  2.8575
26 px -21.32965
27 px  21.32965
28 py -5.2959
29 py  5.2959
30 pz -2.7559
```

```
31 pz   2.7559
c KCl Seed Source
40 px -17.4985
41 px  17.4985
42 py  -4.4070
43 py   4.4070
50 pz  -4.2463
51 pz   4.2463
c Plastic Sleeve
60 px -17.5985
61 px  17.5985
62 py  -4.5070
63 py   4.5070
64 pz  -2.9575
65 pz   2.9575
66 pz  -4.3463
67 pz   4.3463
c Concrete disk
90 cz   250
91 pz  -14.3463
c Point of Know Return
99 so   500
c Blank card follows >>>

c Data Cards
mode p
sdef cel=d1 x=fcel d2 y=fcel d5 z=fcel d8 erg=1.460822 par=2
si1  L 40  41          $ Cell regions used as source
sp1    0.5 0.5         $ Both cells have equal probability
ds2  S 3 4             $ Distributions for sampling along X-direction
si3 -17.4985 17.4985 $ Sampling limits for source 1
sp3  0 1              $ Equal source distribution along X for source 1
si4 -17.4985 17.4985 $ Sampling limits for source 2
sp4  0 1              $ Equal source distribution along X for source 2
ds5  S 6 7             $ Distributions for sampling along Y-direction
si6  -4.4070  4.4070 $ Sampling limits for source 1
sp6  0 1              $ Equal source distribution along Y for source 1
si7  -4.4070  4.4070 $ Sampling limits for source 2
sp7  0 1              $ Equal source distribution along Y for source 2
ds8  S 9 10            $ Distributions for sampling along Z-direction
si9  -4.2463 -2.9575 $ Sampling limits for source 1
sp9  0 1              $ Equal source distribution along Z for source 1
si10  2.9575  4.2463 $ Sampling limits for source 2
sp10 0 1              $ Equal source distribution along Z for source 2
c
c CUT cards
cut:p j 0.02
c
c Material Cards (from PNNL 15870 Rev1, except where noted)
c
c Sodium iodide (3.667 g/cc)
m1   11000  0.5
     53000  0.5
c
c Steel, Stainless 304L (8.00 g/cc)
m2    6000 -0.00015   $ C
     14000 -0.00500   $ Si
     15031 -0.00023   $ P
     16000 -0.00015   $ S
```

```
     24000 -0.19000   $ Cr
     25000 -0.01000   $ Mn
     26000 -0.69448   $ Fe
     28000 -0.10000   $ Ni
c
c Gold (19.3 g/cc)
m3   79000 1.0        $ Au (19.3 g/cc)
c
c Mixture of 92wt% KCl and 8wt% Bi (2.6077 g/cc)
m4   17000 -0.43751   $ Cl
     19000 -0.48249   $ K
     83000 -0.08      $ Bi
c
c Polytetrafluoroethylene (PTFE, Teflon) (2.25 g/cc)
m5    6000 0.333339   $ C
      9019 0.666661   $ F
c
c Air, dry, near sea level (1.205e-3 g/cc)
m6    6000  -0.000124 $ C
      7014  -0.755268 $ N
      8016  -0.231781 $ O
      18000 -0.012827 $ Ar
c
c Concrete (from Ryan) (density 2.301 g/cc)
m7   06000  -0.000500 $ C
     08000  -0.473100 $ O
     11000  -0.020000 $ Na
     12000  -0.003594 $ Mg
     13000  -0.066000 $ Al
     14000  -0.295200 $ S
     19000  -0.032700 $ P
     20000  -0.089800 $ Ca
     25000  -0.001153 $ Mn
     26000  -0.019100 $ Fe
c
c Polypropylene, C3H6 (0.9 g/cc)
m8    1001  -0.143711 $ H
      6000  -0.856289 $ C
c Detector Tallies
c
c Overall Pulse Height Spectrum w/ Gaussian Energy Broadening for Generic NaI
F8:P 10
E8 0 1E-04 0.002 848i 1.7 20.0
FT8 GEB -0.00789 0.06769 0.21159
c
c X-ray Peak PH Spectrum w/ GEB (Gamma, Bi)
F18:P 10
E18 0 1E-04 0.065169 0.089045 1.368290 1.553354 20.0
FT18 GEB -0.00789 0.06769 0.21159
c
c MCNP will run for 1e8 particle histories
nps 1e8
c Blank card follows >>>
```

A.4. Example MCNPX Input Deck for Air Dose in KBMS, Beta Component

```
Dose Calculations for KBMS with 500 g K, 4 wt% Bi (Beta Component)
c                                                                        #
c   Built by:   Jeremy Rogers                                            #
c               Texas A&M University                                     #
c               jl.rogers@tamu.edu                                       #
c                                                                        #
c Plastic-encased KCl/Bi matrix geometry                                 #
c 50 wt% urethane, 46 wt% KCl, 4 wt% Bi matrix (1.8538 g/cc)             #
c
c Cell Cards
10  1 -3.667     10 -11  12 -13  14 -15      imp:e,p=1 $ NaI crystal
11  5 -2.25      26 -27  28 -29  30 -31  & $
                 (-10:11:-12:13:-14:15)      imp:e,p=1 $ Teflon filling
20  2 -8.00      20 -21  22 -23  24 -25  & $
                 (-26:27:-28:29:-30:31)      imp:e,p=1 $ 304L stainless steel
40  4 -1.8538    40 -41  42 -43  50 -24      imp:e,p=1 $ KCl cal source, bottom
41  4 -1.8538    40 -41  42 -43  25 -51      imp:e,p=1 $ KCl cal source, top
70  6 -1.205e-3 -70                          imp:e,p=1 $ Dosimetry spheres
72  6 -1.205e-3 -72                          imp:e,p=1 $
73  6 -1.205e-3 -73                          imp:e,p=1 $
74  6 -1.205e-3 -74                          imp:e,p=1 $
75  6 -1.205e-3 -75                          imp:e,p=1 $
76  6 -1.205e-3 -76                          imp:e,p=1 $
77  6 -1.205e-3 -77                          imp:e,p=1 $
78  6 -1.205e-3 -78                          imp:e,p=1 $
79  6 -1.205e-3 -79                          imp:e,p=1 $
80  6 -1.205e-3 -80                          imp:e,p=1 $
81  6 -1.205e-3 -81                          imp:e,p=1 $
c 90  7 -2.301    -90 -50  91                imp:e,p=1 $ Concrete
99  6 -1.205e-3 #10 #11 #20 #40 #41  70      & $
                 72  73  74  75  76  77  78  & $
                 79  80  81                 -99 imp:e,p=1 $ Surrounding void
100 0                                        99 imp:e,p=0 $ Point of Know Return
c Blank card follows >>>

c Surface Cards
c NaI crystal
10 px -20.32
11 px  20.32
12 py -5.08
13 py  5.08
14 pz -2.54
15 pz  2.54
c S/S housing, PMT excluded
20 px -21.43125
21 px  21.43125
22 py -5.3975
23 py  5.3975
24 pz -2.8575
25 pz  2.8575
26 px -21.32965
27 px  21.32965
28 py -5.2959
29 py  5.2959
30 pz -2.7559
31 pz  2.7559
c KCl Cal Source
```

97

```
40 px -17.4985
41 px  17.4985
42 py  -4.4070
43 py   4.4070
50 pz  -4.6704
51 pz   4.6704
c Dosimetry spheres
70 sz   4.7704  0.05  $ center 1 mm from cal source
72 sz   5.6704  0.5   $ 1 cm from cal source
73 sz   7.2104  1.0   $ 1 in from cal source
74 sz   9.7504  1.0   $ 2 in from cal source
75 sz  14.8304 1.0    $ 4 in from cal source
76 sz  19.9104 1.0    $ 6 in from cal source
77 sz  27.5304 1.0    $ 9 in from cal source
78 sz  35.1504 1.0    $ 12 in from cal source
79 sz  50.3904 1.0    $ 18 in from cal source
80 sz  65.6304 1.0    $ 24 in from cal source
81 sz  104.6704 1.0 $ 1 m from cal source
c Concrete disk
c 90 cz   250
c 91 pz  -14.6704
c Point of Know Return
99 so   500
c Blank card follows >>>

c Data Cards
mode p e
sdef x=d1 y=d2 z=d3 erg=d4 par=3
si1 -17.4985 17.4985 $ Sampling limits
sp1  0 1              $ Equal source distribution along X
si2  -4.4070  4.4070  $ Sampling limits
sp2  0 1              $ Equal source distribution along Y
si3   2.8575  4.6704  $ Sampling limits
sp3  0 1              $ Equal source distribution along Z
si4  H 0 3.28E-02 9.84E-02 1.64E-01 2.30E-01 2.95E-01 $ Beta Source Histogram
         3.61E-01 4.26E-01 4.92E-01 5.57E-01 6.23E-01
         6.89E-01 7.54E-01 8.20E-01 8.85E-01 9.51E-01
         1.02E+00 1.08E+00 1.15E+00 1.21E+00 1.28E+00
sp4  D 0 2.96E-02 3.70E-02 4.34E-02 4.89E-02 5.35E-02 $ Beta Probability Dist.
         5.71E-02 5.99E-02 6.17E-02 6.26E-02 6.25E-02
         6.14E-02 5.92E-02 5.61E-02 5.18E-02 4.62E-02
         3.92E-02 3.05E-02 2.03E-02 1.00E-02 1.83E-03
c
c CUT cards
cut:e j 0.02
cut:p j 0.02
c
c Material Cards (from PNNL 15870 Rev1, except where noted)
c Sodium iodide (3.667 g/cc)
m1   11000  0.5
     53000  0.5
c
c Steel, Stainless 304L (8.00 g/cc)
m2    6000 -0.00015   $ C
     14000 -0.00500   $ Si
     15031 -0.00023   $ P
     16000 -0.00015   $ S
     24000 -0.19000   $ Cr
     25000 -0.01000   $ Mn
```

```
     26000 -0.69448   $ Fe
     28000 -0.10000   $ Ni
c
c Gold (19.3 g/cc)
m3   79000 1.0        $ Au (19.3 g/cc)
c
c Mixture of 46wt% KCl and 4wt% Bi with 50wt% urethane binder (1.8538 g/cc)
m4    1000 -0.03960   $ H
      6000 -0.20222   $ C
      7000 -0.07861   $ N
      8000 -0.17958   $ O
     17000 -0.21400   $ Cl
     19000 -0.23600   $ K
     83000 -0.05      $ Bi
c
c Polytetrafluoroethylene (PTFE, Teflon) (2.25 g/cc)
m5    6000 0.333339   $ C
      9019 0.666661   $ F
c
c Air, dry, near sea level (1.205e-3 g/cc)
m6    6000  -0.000124 $ C
      7014  -0.755268 $ N
      8016  -0.231781 $ O
      18000 -0.012827 $ Ar
c
c Concrete (from Ryan) (density 2.301 g/cc)
m7    06000  -0.000500 $ C
      08000  -0.473100 $ O
      11000  -0.020000 $ Na
      12000  -0.003594 $ Mg
      13000  -0.066000 $ Al
      14000  -0.295200 $ S
      19000  -0.032700 $ P
      20000  -0.089800 $ Ca
      25000  -0.001153 $ Mn
      26000  -0.019100 $ Fe
c
c Polypropylene, C3H6 (0.9 g/cc)
m8    1001  -0.143711 $ H
      6000  -0.856289 $ C
c
c Water, Liquid (1.0 g/cc)
m9    1001  0.666657 $ H
      8016  0.333343 $ O
c
c Detector Tallies
c
c Electron Net Current at Outer Surface of Cal Source
c    Both outward and inward current are calculated; their difference is net
F1:E 51
E1 0 0.1 11i 1.3
C1 0 1.0
c
c Overall Pulse Height Spectrum w/ Gaussian Energy Broadening for Generic NaI
F8:P 10
E8 0 1E-04 0.002 348i 0.7
FT8 GEB -0.00789 0.06769 0.21159
c
c X-ray Peak PH Spectrum w/ GEB
```

```
F18:P 10
E18 0 1E-04 0.065169 0.089045 0.7
FT18 GEB -0.00789 0.06769 0.21159
c
c Detector Dose Tally
c Dose in tissue calculated at 1mm (contact), 1cm, 1in, 2in, 4in, 6in, 9in,
12in,
c    18in, 24in, and 1m
F5:P 0 0 4.7704 0.05    0 0 5.6704 1.0    0 0 7.2104 1.0    0 0 9.7504 1.0    &
$
     0 0 14.8304 1.0    0 0 19.9104 1.0    0 0 27.5304 1.0    0 0 35.1504 1.0   &
$
     0 0 50.3904 1.0    0 0 65.6304 1.0    0 0 104.6704 1.0
DF5 ic=31
c
c Cell Energy Deposition Tally
F6:E 70 72 73 74 75 76 77 78 79 80 81
E6   0 0.1 11i 1.3
c
c Dosimeter Energy Deposition Tally
*F28:E 70 72 73 74 75 76 77 78 79 80 81
E28 0 0.01 8i 0.1 1.3
c
c Energy Deposition Tally for Reference Dosimeter (1 foot from source)
*F38:E 78
E38 0 0.01 8i 0.1 1.3
c
c MCNP will run for 5e8 particle histories
nps 5e8
c Blank card follows >>>
```

A.5. Example MCNP Input Deck for Weak Concrete Background Source

```
Weak Background Source Term for 500 g K KBM Source, 4 wt% Bi (Gamma Component)
c                                                                           #
c   Built by:    Jeremy Rogers                                              #
c                Texas A&M University                                       #
c                jl.rogers@tamu.edu                                         #
c                                                                           #
c Plastic-encased KCl/Bi matrix geometry                                    #
c 50 wt% urethane, 46 wt% KCl, 4 wt% Bi matrix (1.8538 g/cc)                #
c Background source is Ryan F1                                              #
c
c Cell Cards
10  1 -3.67     10 -11  12 -13  14 -15    imp:e,p=1 $ NaI crystal
11  5 -2.2      26 -27  28 -29  30 -31
                (-10:11:-12:13:-14:15)    imp:e,p=1 $ Teflon filling
20  2 -8.03     20 -21  22 -23  24 -25
                (-26:27:-28:29:-30:31)    imp:e,p=1 $ 304L stainless steel
40  4 -1.8538   40 -41  42 -43 -24  44    imp:e,p=1 $ KCl cal source
90  7 -2.301   -90 -44  91                imp:e,p=1 $ Concrete
99  6 -0.001025 #10 #11 #20 #40 #90 -99  imp:e,p=1 $ Surrounding void
100 0          99                         imp:e,p=0 $ Outside world
c Blank card follows >>>

c Surface Cards
c NaI crystal
10 px -20.32
11 px  20.32
12 py -5.08
13 py  5.08
14 pz -2.54
15 pz  2.54
c S/S housing, PMT excluded
20 px -21.43125
21 px  21.43125
22 py -5.3975
23 py  5.3975
24 pz -2.8575
25 pz  2.8575
26 px -21.32965
27 px  21.32965
28 py -5.2959
29 py  5.2959
30 pz -2.7559
31 pz  2.7559
c KCl Seed Source
40 px -17.4985
41 px  17.4985
42 py  -4.4070
43 py   4.4070
44 pz  -6.4832
c Concrete disk
90 cz   250
91 pz  -16.4832
c Encapsulating sphere
99 so  5000
c Blank card follows >>>

c Data Cards
```

```
mode p
sdef axs=0 0 1 ext=d1 rad=d2 vec=0 0 1 dir=d3 erg=d4 par=2
si1 -16.4832 -6.4832
sp1 -21 0
si2 0 250
sp2 -21 1
si3 -1 0 1
sp3 0 0.5 0.5
sb3 0 0.1 0.9
si4 L 0.06329 0.09260 0.12907 0.18621 0.23863 0.24200
       0.27024 0.27736 0.29522 0.30009 0.32803 0.33832
       0.35193 0.40946 0.46300 0.58319 0.60931 0.72733
       0.76836 0.79495 0.86056 0.91120 0.93406 0.96477
       0.96897 1.12039 1.23811 1.37767 1.46081 1.76449
       2.20421 2.61453
sp4 D 0.01800 0.02088 0.00354 0.01128 0.06332 0.02335
       0.00506 0.00332 0.06065 0.00480 0.00431 0.01648
       0.11815 0.00281 0.00643 0.04441 0.14486 0.01502
       0.01552 0.00621 0.00652 0.03773 0.00952 0.00730
       0.02310 0.04745 0.01819 0.01257 0.13276 0.04839
       0.01596 0.05211
c
c CUT cards
cut:p j 0.02
c
c
c Material Cards (from PNNL 15870 Rev1, except where noted)
c Sodium iodide (3.667 g/cc)
m1   11000  0.5
     53000  0.5
c
c Steel, Stainless 304L (8.00 g/cc)
m2    6000 -0.00015   $ C
     14000 -0.00500   $ Si
     15031 -0.00023   $ P
     16000 -0.00015   $ S
     24000 -0.19000   $ Cr
     25000 -0.01000   $ Mn
     26000 -0.69448   $ Fe
     28000 -0.10000   $ Ni
c
c Gold (19.3 g/cc)
m3   79000 1.0        $ Au (19.3 g/cc)
c
c Mixture of 92wt% KCl and 8wt% Bi (2.6077 g/cc)
m4   17000 -0.43751   $ Cl
     19000 -0.48249   $ K
     83000 -0.08      $ Bi
c
c Polytetrafluoroethylene (PTFE, Teflon) (2.25 g/cc)
m5    6000 0.333339   $ C
      9019 0.666661   $ F
c
c Air, dry, near sea level (1.205e-3 g/cc)
m6    6000 -0.000124 $ C
      7014 -0.755268 $ N
      8016 -0.231781 $ O
     18000 -0.012827 $ Ar
c
```

```
c Concrete (from Ryan) (density 2.301 g/cc)
m7   06000  -0.000500 $ C
     08000  -0.473100 $ O
     11000  -0.020000 $ Na
     12000  -0.003594 $ Mg
     13000  -0.066000 $ Al
     14000  -0.295200 $ S
     19000  -0.032700 $ P
     20000  -0.089800 $ Ca
     25000  -0.001153 $ Mn
     26000  -0.019100 $ Fe
c
c Polypropylene, C3H6 (0.9 g/cc)
m8    1001  -0.143711 $ H
      6000  -0.856289 $ C
c
c Detector Tallies
c
c Overall Pulse Height Spectrum w/ Gaussian Energy Broadening for Generic NaI
F8:P 10
E8 0 1E-04 0.002 848i 1.7 20.0
FT8 GEB -0.00789 0.06769 0.21159
c
c X-ray Peak PH Spectrum w/ GEB (Gamma, Bi)
F18:P 10
E18 0 1E-04 0.065169 0.089045 20.0
FT18 GEB -0.00789 0.06769 0.21159
c MCNP will run for 5e8 particles
nps 5e8
c Blank card follows >>>
```

A.6.   Example MCNPX Source Definition Cards, Strong Background Source

```
C Strong Concrete Background (Ryan G1), Source Definition
sdef axs=0 0 1 ext=d1 rad=d2 vec=0 0 1 dir=d3 erg=d4 par=2
si1 -16.4832 -6.4832
sp1 -21 0
si2 0 250
sp2 -21 1
si3 -1 0 1
c Source Biasing
sp3 0 0.5 0.5
sb3 0 0.1 0.9
si4 L 0.06329 0.09260 0.12907 0.18621 0.23863 0.24200  $ Gamma Emission Lines
       0.27024 0.27736 0.29522 0.30009 0.32803 0.33832
       0.35193 0.40946 0.46300 0.58319 0.60931 0.72733
       0.76836 0.79495 0.86056 0.91120 0.93406 0.96477
       0.96897 1.12039 1.23811 1.37767 1.46081 1.76449
       2.20421 2.61453
sp4 D 0.00656 0.00761 0.00550 0.00655 0.09843 0.01355  $ Emission Prob. Dist.
       0.00787 0.00516 0.03519 0.00746 0.00671 0.02562
       0.06856 0.00436 0.01000 0.06904 0.08405 0.02335
       0.00901 0.00966 0.01014 0.05865 0.00552 0.01134
       0.03592 0.02753 0.01056 0.00729 0.21047 0.02808
       0.00926 0.08102
```